Physics of Fluids manuscript No.
(will be inserted by the editor)

An immersed phase field fracture model for microporomechanics with Darcy-Stokes flow

Hyoung Suk Suh (서형석) · WaiChing Sun (孫維正)

Received: December 14, 2020/ Accepted: date

Abstract This paper presents an immersed phase field model designed to predict the fracture-induced flow due to brittle fracture in vuggy porous media. Due to the multiscale nature of pores in vuggy porous material, crack growth may connect previously isolated pores which lead to flow conduits. This mechanism has important implications for many applications such as disposal of carbon dioxide and radioactive materials, hydraulic fracture and mining. To understand the detailed microporomechanics that causes the fracture-induced flow, we introduce a new phase field fracture framework where the phase field is not only used as an indicator function for damage of the solid skeleton, but also as an indicator of the pore space. By coupling the Stokes equation that governs the fluid transport in the voids, cavities and cracks, and the Darcy's flow in the deformable porous media, our proposed model enables us to capture the fluid-solid interaction of the pore fluid and solid constituents during the crack growth. Numerical experiments are conducted to analyze how presence of cavities affects the accuracy of the predictions based on homogenized effective medium during crack growth.

Keywords Biot-Stokes model, coupled Stokes-Darcy flow, vuggy porous media, immersed phase field, brittle fracture

1 Introduction

Geomaterials such as carbonate rocks, sandstone or limestone often contain geometrical features such as cracks, joints, vugs or cavities. When the defects are partially or fully saturated with pore fluid, the geometry of the features may affect effective stiffness, permeability, water retention characteristics and drained or undrained shear strength of the material [Juanes et al., 2006, Sun et al., 2011b, Kang et al., 2016, Suh et al., 2017, Selvadurai et al., 2017, Wang and Sun, 2017, Sun and Wong, 2018]. Furthermore, brittle fracture in materials that possess geometrical features may lead to pore fluid in cavities migrate into the flow channels and cause flow conduits that lead to often undesirable outcomes. Modeling geometrical features in porous media are thus highly important and at the same time challenging subject for the hydromechanically coupled analysis in geomechanics problems like hydrocarbon resources recovery or development of enhanced geothermal energy reservoirs [Paterson and Fermigier, 1997, Class et al., 2002, Rutqvist et al., 2007, Grant, 2013, Wagner et al., 2015, Heider and Markert, 2017, Suh and Sun, 2020].

One possible modeling choice is to consider a fictitious effective medium at a scale where representative elementary volume exists. In this case, the geometrical features of the material are not explicitly modeled but the influences of the these geometrical features are incorporated in the constitutive relations by treating defects as a different pore system that interacts with the matrix pores [Choo and Borja, 2015, Choo et al., 2016, Liu and Abousleiman, 2017, Wang and Sun, 2018]. The upshot of the multi-porosity and

Corresponding author: WaiChing Sun
Associate Professor, Department of Civil Engineering and Engineering Mechanics, Columbia University, 614 SW Mudd, Mail Code: 4709, New York, NY 10027 Tel.: 212-854-3143, Fax: 212-854-6267, E-mail: wsun@columbia.edu

multi-permeability models is mainly the simple numerical treatment since there is no need for complex meshing techniques or embedded strong discontinuities, and the computational efficiency compared to pore-scale models that require extremely large domain in order to reproduce hydromechanical behavior at large scales [Ghaboussi and Barbosa, 1990, Spaid and Phelan Jr, 1997, Blunt et al., 2002, Tang et al., 2005, Arson and Pereira, 2013, Pereira and Arson, 2013, Suh and Yun, 2018]. However, the drawback of this approach is that the homogenized effective medium may not sufficiently represent the microstructural details. This makes the identification of material parameters more complicated since the effective permeability of multiple interacting systems are not isotropic and the constitutive law for the fluid mass exchanges inherently depends on the microstructure.

Another common alternative to model the interaction between the cavities and the crack growth is to conduct simulations via a fracture network model [Ozkan et al., 2010, Leung and Zimmerman, 2012, Fu et al., 2013, Hyman et al., 2015]. However, the obvious drawback is that the fracture in those models must either be straight line (in the two-dimensional case) or a plane (in the three-dimensional case) and hence the geometrical effect on the porous media can not be captured precisely.

In this research, we introduce a phase field framework that allows us to enable a unified treatment to simulate the evolving geometry of cracks and the cavities. By introducing the phase field as an unified representation of the void space that is not suitable to be treated as as an effective medium, we introduce a framework that enables us to analyze how crack propagation in vuggy porous media may affect the flow mechanism differently than the porous media with pores well distributed in the host matrix. Our result indicates that interaction between the propagating cracks of the cavities is important for capturing the hydromechanical responses of the porous media and that existing effective medium approach which characterizes the pore space with a single hydraulic model such as cubic law and Kozeny-Carmen model may not be sufficient to capture the cavity-crack-host-matrix interactions.

As for notations and symbols, bold-faced and blackboard bold-faced letters denote tensors (including vectors which are rank-one tensors); the symbol '$\cdot$' denotes a single contraction of adjacent indices of two tensors (e.g., $\boldsymbol{a} \cdot \boldsymbol{b} = a_i b_i$ or $\boldsymbol{c} \cdot \boldsymbol{d} = c_{ij} d_{jk}$); the symbol ':' denotes a double contraction of adjacent indices of tensor of rank two or higher (e.g., $\mathbb{C} : \boldsymbol{\varepsilon} = C_{ijkl}\varepsilon_{kl}$); the symbol '$\otimes$' denotes a juxtaposition of two vectors (e.g., $\boldsymbol{a} \otimes \boldsymbol{b} = a_i b_j$) or two symmetric second order tensors [e.g., $(\boldsymbol{\alpha} \otimes \boldsymbol{\beta})_{ijkl} = \alpha_{ij}\beta_{kl}$]. We also define identity tensors: $\boldsymbol{I} = \delta_{ij}$ and $\mathbb{I} = \delta_{ik}\delta_{jl}$, where δ_{ij} is the Kronecker delta. As for sign conventions, unless specified, the directions of the tensile stress and dilative pressure are considered as positive.

2 The model problem

We consider a fully saturated Biot-Stokes system (Fig. 1) that consists of two regions (intact porous matrix $\mathcal{B}_D$, and cracks or cavities $\mathcal{B}_S$) separated by the sharp interface Γ^*, where we assume that the solid phase in $\mathcal{B}_D$ forms a deformable porous matrix while solid particles in $\mathcal{B}_S$ are in suspension. In this case, both the solid and fluid phases coexist in both regions. By considering our material of interest as a multi-phase continuum, we utilize the effective stress principle for the intact porous matrix where the fluid flow is modeled with the Darcy's law, while the motion of solid-fluid mixture is modeled by the Stokes equation [Li et al., 2018]. Two distinct regions are then coupled by properly imposing three transmissibility conditions at the interface. The model problem with the sharp interface will be later on extended into a diffuse Biot-Stokes model by introducing the phase field in Section 3.

2.1 Continuum representation

Although Biot-Stokes system only contains two immiscible solid and fluid phases, for mathematical convenience, we idealize the material of interest as a three-phase continuum where each constituent [i.e., solid (s), pore fluid (f_D), and free fluid (f_S)] occupies a fraction of volume at the same material point. By letting $dV = dV_s + dV_f$ denote the representative elementary volume of the material, we define the volume fractions for the constituents as,

$$\phi^\alpha := \frac{dV_\alpha}{dV} \; ; \; \alpha = \{s, f\} \, , \tag{1}$$

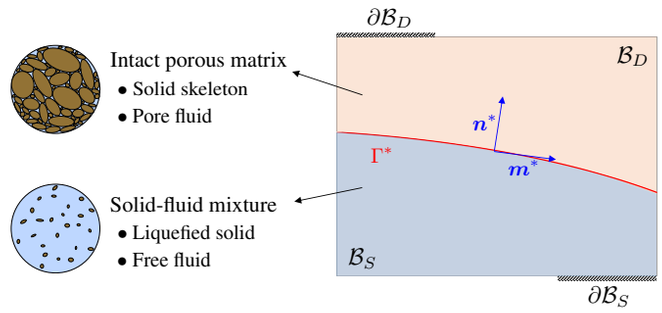

Fig. 1: Schematic representation of Biot-Stokes system that possesses sharp interface Γ^*.

where the index s refer to the solid phase and f indicates the fluid phase. Since the sharp interface separates our system of interest into two regions, the volume fraction of the pore and free fluids can be expressed as:

$$\phi^f = \underbrace{(1 - H_{\Gamma^*})\frac{dV_{f_D}}{dV}}_{:=\phi^{f_D}} + \underbrace{H_{\Gamma^*}\frac{dV_{f_S}}{dV}}_{:=\phi^{f_S}}, \tag{2}$$

where H_{Γ^*} is the Heaviside function that satisfies,

$$H_{\Gamma^*} = \begin{cases} 0 & \text{in } \mathcal{B}_D, \\ 1 & \text{in } \mathcal{B}_S. \end{cases} \tag{3}$$

In addition, by letting ρ_s and ρ_f denote the intrinsic mass densities of solid and fluid, respectively, the partial mass densities for each constituent (ρ^α, where $\alpha = s, f_D, f_S$) are given by,

$$\rho^s := \phi^s\rho_s \ ; \ \rho^{f_D} := \phi^{f_D}\rho_f \ ; \ \rho^{f_S} := \phi^{f_S}\rho_f \ ; \ \rho := \rho^s + \rho^{f_D} + \rho^{f_S}, \tag{4}$$

where ρ is the mass density of the entire system. In this study, we assume that both the solid and fluid phases are incompressible, so that intrinsic mass densities ρ_s and ρ_f are considered as constants.

2.2 Governing equations

This section briefly reviews the balance principles, constitutive laws in the bulk volume of a porous medium (Section 2.2.1), the region where solid-fluid mixture flows freely (Section 2.2.2), and the sharp interface between two regions (Section 2.2.3).

2.2.1 Conservation laws for an intact porous matrix

For the region where the solid forms an intact porous matrix, we adopt the effective stress principle [Lade and De Boer, 1997, Borja, 2006] so that the external loading imposed on the matrix is assumed to be carried by both the solid skeleton and the pore fluid. In this case, the region $\mathcal{B}_D$ is governed by the following system of equations [Borja and Alarcón, 1995, White and Borja, 2008, Sun et al., 2013]:

$$\nabla\cdot(\boldsymbol{\sigma}' - Bp_{f_D}\boldsymbol{I}) + \rho\boldsymbol{g} = \boldsymbol{0} \text{ in } \mathcal{B}_D, \tag{5}$$

$$\nabla\cdot\boldsymbol{v}_s + \nabla\cdot\boldsymbol{w}_{f_D} + \frac{1}{M}\dot{p} = 0 \text{ in } \mathcal{B}_D, \tag{6}$$

where $\boldsymbol{\sigma}'$ is the effective stress, $B = 1 - K/K_s$ is the Biot's coefficient, M is the Biot's modulus, p_{f_D} is the pore pressure, $\boldsymbol{g}$ is the gravitational acceleration, $\boldsymbol{v}_\alpha$ is the intrinsic velocity of constituent α, and $\boldsymbol{w}_{f_D} = \phi^{f_D}(\boldsymbol{v}_{f_D} - \boldsymbol{v}_s)$ is the Eulerian relative flow vector of the pore fluid (i.e., Darcy's velocity). Here, we assume

that $B \approx 1$ and $1/M \approx 0$ to simplify the formulation. Note that the Biot's coefficient of many sandstone and shale specimens are often less than one, whereas it is more reasonable to assume Biot's coefficient equal to 1 for granite (e.g. Westerly granite) [Berryman and Wang, 1995, Zimmerman, 2000, Jaeger et al., 2009]. In either cases, the damage of the solid skeleton may reduce the elastic bulk modulus of the solid skeleton. Therefore both the Biot's coefficient and modulus may evolve according to the solid deformation. This nonlinear effect is not considered in this study but will be considered in the future. We also assume that the behavior of intact matrix in $\mathcal{B}_D$ is linear and isotropic elastic and hence only two independent elastic modulii are needed to capture the elastic response. The constitutive relation for the solid skeleton can therefore be written as follows:

$$\boldsymbol{\sigma}_0' = \lambda \, \mathrm{tr}\,(\boldsymbol{\varepsilon})\boldsymbol{I} + 2\mu\boldsymbol{\varepsilon} \text{ in } \mathcal{B}_D, \tag{7}$$

where $\boldsymbol{\sigma}_0'$ indicates the effective stress of the undamaged matrix. The actual and undamaged effective stress are related by a degradation function, which will later be discussed in Section 3.2. Furthermore, $\boldsymbol{\varepsilon} = (\nabla \boldsymbol{u}_s + \nabla \boldsymbol{u}_s^{\mathrm{T}})/2$ is the infinitesimal solid strain tensor that depends on the solid displacement $\boldsymbol{u}_s$, and parameters λ and μ are the Lamé constants. For the constitutive equation that describes laminar pore fluid flow in $\mathcal{B}_D$, we use the generalized Darcy's law that linearly relates the relative velocity $\boldsymbol{w}_{f_D}$ and pore pressure gradient ∇p_{f_D}, i.e.,

$$\boldsymbol{w}_{f_D} = -\frac{k}{\mu_f}(\nabla p_{f_D} - \rho_f \boldsymbol{g}) \text{ in } \mathcal{B}_D, \tag{8}$$

where μ_f is the dynamic viscosity of the pure fluid phase, and k is the effective permeability of the porous matrix. Additionally, in order to incorporate the effect of deformation of the matrix on the porous medium flow [Mauran et al., 2001, Schutjens et al., 2004], this study adopts the Kozeny-Carman equation to empirically capture the porosity-permeability relation [Chapuis and Aubertin, 2003, Costa, 2006, Wang and Sun, 2017]. Note that the Kozeny-Carmen equation is often considered a rough approximation of the porosity-permeability relation. A more precise predictions of permeability may requires new geometrical attributes such as tortuosity [Sun et al., 2011b,a], formation factor [Worthington, 1993, Sun and Wong, 2018], and percolation threshold [Mavko and Nur, 1997]. This extension is out of the scope of this study but will be considered in future work.

Recall Section 2.1 that $\phi^s + \phi^{f_D} = 1$ in $\mathcal{B}_D$. Then, by letting $\phi := \phi^{f_D}$ the porosity of the matrix, the Kozeny-Carman equation reads,

$$k = k_0 \left[\frac{(1-\phi_0)^2}{\phi_0^3}\right]\left[\frac{\phi^3}{(1-\phi)^2}\right] \text{ in } \mathcal{B}_D, \tag{9}$$

where k_0 and ϕ_0 denote the reference permeability and porosity, respectively.

2.2.2 *Conservation laws for solid-fluid mixture*

This study attempts to model suspension flow in $\mathcal{B}_S$, where mass and linear momentum balances for both solid and fluid phases should be satisfied. We therefore write the governing balance equations for $\mathcal{B}_S$ as,

$$\nabla \cdot \boldsymbol{\sigma}^{f_S} + \rho^{f_S}\boldsymbol{g} = \boldsymbol{0} \text{ in } \mathcal{B}_S, \tag{10}$$

$$\nabla \cdot \boldsymbol{\sigma}^{s} + \rho^{s}\boldsymbol{g} = \boldsymbol{0} \text{ in } \mathcal{B}_S, \tag{11}$$

$$\nabla \cdot \boldsymbol{v}_s + \nabla \cdot \boldsymbol{w}_{f_S} = 0 \text{ in } \mathcal{B}_S, \tag{12}$$

where $\boldsymbol{\sigma}^{\alpha}$ is the Cauchy stress tensor of α constituent, and the relative flow vector of the free fluid can be defined as $\boldsymbol{w}_{f_S} = \phi^{f_S}(\boldsymbol{v}_{f_S} - \boldsymbol{v}_s)$. By assuming that the free fluid resides in $\mathcal{B}_S$ with low Reynolds number (i.e., $Re \ll 1$), we adopt a simplified version of the Navier-Stokes model, i.e., the Stokes equation. The Stokes model for the steady-state motion of an incompressible fluid yields the following relationship for the free fluid stress tensor $\boldsymbol{\sigma}^{f_S}$ as,

$$\boldsymbol{\sigma}^{f_S} = -p_{f_S}\boldsymbol{I} + \mu_{\mathrm{eff}}(\nabla \boldsymbol{v}_{f_S} + \nabla \boldsymbol{v}_{f_S}^{\mathrm{T}}) \text{ in } \mathcal{B}_S, \tag{13}$$

where p_{f_S} is the free fluid pressure and μ_{eff} is the effective viscosity of the solid-fluid mixture [Mooney, 1951, Cheng and Law, 2003], i.e.,

$$\mu_{\text{eff}} = \mu_f \exp\left(\frac{2.5c}{1 - c/c_{\max}}\right) \text{ in } \mathcal{B}_S, \tag{14}$$

where $c := 1 - \phi^{f_S}$ indicates the solid particle concentration, and $c_{\max}$ denotes its upper bound. Again, notice that we introduce only one solid constituent for the entire system since it is convenient for us to later on impose interface conditions and further adopt the phase field fracture model that simulates evolving interface. This approach may not be suitable for modeling complete suspension flow where $\boldsymbol{v}_s = \boldsymbol{v}_{f_S}$. However, we assume that solid particles in $\mathcal{B}_S$ follows the same constitutive relations as the free fluid in order to replicate the suspension flow as close as possible, i.e.,

$$\boldsymbol{\sigma}^s = -p_{f_S}\boldsymbol{I} + \mu_{\text{eff}}(\nabla \boldsymbol{v}_s + \nabla \boldsymbol{v}_s^{\text{T}}) \text{ in } \mathcal{B}_S. \tag{15}$$

2.2.3 Conservation laws for the sharp interface between intact matrix and solid-fluid mixture

In order to properly model the interaction between the porous matrix ($\mathcal{B}_D$) and the vugs or cavities ($\mathcal{B}_S$), complete mass conservation and force equilibrium for the entire system should be satisfied. Since we have two different constituents for the same type of fluid (f_D and f_S) while considering only one solid constituent (s), coupling two subsystems thus requires the enforcement of fluid transmissibility conditions at the sharp interface Γ^* that models the coupled Stokes-Darcy flow [Arbogast and Lehr, 2006, Arbogast and Brunson, 2007, Badia et al., 2009, Wu and Mirbod, 2018, Bergkamp et al., 2020].

The first interface condition is the fluid continuity that ensures the mass conservation. Since we assume that the fluid phase is incompressible, the interfacial fluid fuxes for each subsystem ($\mathcal{M}^*_{f_D}$ and $\mathcal{M}^*_{f_S}$) can be expressed as follows:

$$\mathcal{M}^*_{f_D} = \int_{\Gamma^*} \underbrace{\boldsymbol{w}_{f_D} \cdot \boldsymbol{n}^*_D}_{:=m^*_{f_D}} \, d\Gamma \ ; \ \mathcal{M}^*_{f_S} = \int_{\Gamma^*} \underbrace{\boldsymbol{w}_{f_S} \cdot \boldsymbol{n}^*_S}_{:=m^*_{f_S}} \, d\Gamma, \tag{16}$$

where $\boldsymbol{n}^*_D$ and $\boldsymbol{n}^*_S$ denote the outward-oriented normal vectors from $\mathcal{B}_D$ and $\mathcal{B}_S$, respectively. From Eq. (16), mass continuity ($\mathcal{M}^*_{f_D} + \mathcal{M}^*_{f_S} = m^*_{f_D} + m^*_{f_S} = 0$) yields the following transmissibility condition:

$$\boldsymbol{w}_{f_D} \cdot \boldsymbol{n}^*_D + \boldsymbol{w}_{f_S} \cdot \boldsymbol{n}^*_S = (\boldsymbol{w}_{f_S} - \boldsymbol{w}_{f_D}) \cdot \boldsymbol{n}^* = 0 \text{ on } \Gamma^*, \tag{17}$$

where we take $\boldsymbol{n}^* = \boldsymbol{n}^*_S = -\boldsymbol{n}^*_D$ for notational convenience (Fig. 1). Here, Eq. (16) implies that the normal component of the fluid velocities ($\boldsymbol{w}_{f_S}$ and $\boldsymbol{w}_{f_D}$) should be identical in order to guarantee that the exchange of fluid mass between $\mathcal{B}_S$ and $\mathcal{B}_D$ is conservative.

The second condition is the force equilibrium at the interface Γ^*. From each subsystem, total forces acting on the interface ($\boldsymbol{\mathcal{F}}^*_{f_D}$ and $\boldsymbol{\mathcal{F}}_{f_S}$) may be written as,

$$\boldsymbol{\mathcal{F}}^*_{f_D} = \int_{\Gamma^*} \underbrace{p_{f_D}\boldsymbol{n}^*}_{:=\boldsymbol{t}^*_{f_D}} \, d\Gamma \ ; \ \boldsymbol{\mathcal{F}}^*_{f_S} = \int_{\Gamma^*} \underbrace{\boldsymbol{\sigma}^{f_S} \cdot \boldsymbol{n}^*}_{:=\boldsymbol{t}^*_{f_S}} \, d\Gamma, \tag{18}$$

where $\boldsymbol{t}^*_{f_D}$ and $\boldsymbol{t}^*_{f_S}$ indicate the tractions at the interface. The force equilibrium requires $\boldsymbol{\mathcal{F}}^*_{f_D} + \boldsymbol{\mathcal{F}}^*_{f_S} = \boldsymbol{t}^*_{f_D} + \boldsymbol{t}^*_{f_S} = \boldsymbol{0}$, implying that the normal and shear components should be balanced at the same time. By decomposing the traction vectors as,

$$\boldsymbol{t}^*_i = (\boldsymbol{t}^*_i \cdot \boldsymbol{n}^*)\boldsymbol{n}^* + \sum_{j=1}^{2}(\boldsymbol{t}^*_i \cdot \boldsymbol{m}^*_j)\boldsymbol{m}^*_j \ ; \ i = \{f_D, f_S\}, \tag{19}$$

where $\boldsymbol{m}_1^*$ and $\boldsymbol{m}_2^*$ are the interfacial tangent vectors, we get two more transmissibility conditions that describe normal and shear force equilibrium, respectively:

$$\boldsymbol{t}_{f_S}^* \cdot \boldsymbol{n}^* + p_{f_D} = 0 \text{ on } \Gamma^*, \tag{20}$$

$$\boldsymbol{t}_{f_S}^* \cdot \boldsymbol{m}_j^* + \mu_f \frac{\alpha_{SD}}{\sqrt{k}} (\boldsymbol{w}_{f_S} - \boldsymbol{w}_{f_D}) \cdot \boldsymbol{m}_j^* = 0 \text{ on } \Gamma^*. \tag{21}$$

Eq. (21) is the Beavers-Joseph-Saffman condition [Beavers and Joseph, 1967, Saffman, 1971, Layton et al., 2002, Arbogast and Brunson, 2007]. This idealized condition relates the slip velocity and the shear stress through the dimensionless slippage coefficient α_{SD}, which depends on the microstructural attributes of the interfaces, such as surface roughness, irregular patterns, as well as the flow velocity [Beavers and Joseph, 1967, Terzis et al., 2019, Guo et al., 2020]. The validity and limitations of the Beavers-Joseph-Saffman condition are documented in a number of literature such as Auriault [2010], Mikelic and Jäger [2000], Monchiet et al. [2019] and will not repeated here. Possible extensions of the interface conditions to turbulent and multiphase flows are an active research area that is clearly out of the scope of this study but will be considered in the future.

3 The phase field Biot-Stokes model with evolving fractures

This section introduces the mathematical model that uses smooth implicit function, i.e., the phase field, to approximate evolving sharp interfaces due to damage. We first review the general procedure that employs an implicit function to approximate sharp interfaces (Section 3.1) shown in Fig. 2. Since the phase field is a smooth representation of the Heaviside function, we derive the corresponding mathematical model that approximates interfacial transmissibility conditions suitable for the diffuse representation of the interface. To capture crack growth according to the Griffith's theory, we adopt the classical variational fracture model to allow crack growth represented by the evolution of the phase field defined over the spatial domain (Section 3.2). These techniques are then applied into the derivation shown in Section 3.3 in which a mathematical model to capture the hydromechanical coupling of pore fluid flows in both the host matrix and evolving interfaces in brittle porous media. The resultant model does not require locally defined enrichment function or remeshing and can be implemented in a standard finite element or finite element/volume solver.

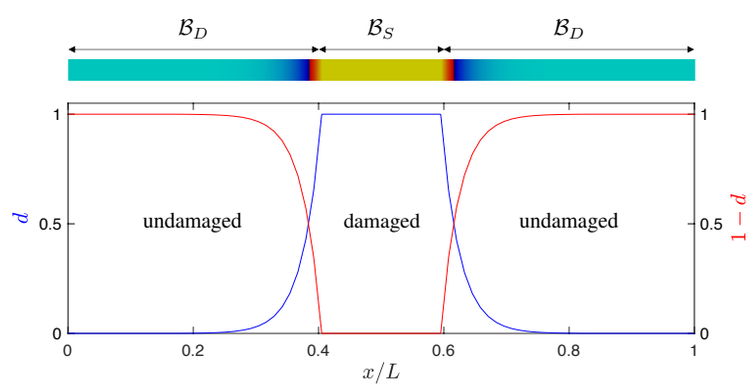

Fig. 2: Diffuse representation of the interface where exemplary 1D domain consists of $\mathcal{B}_S$ in $x/L \in [0.4, 0.6]$ sandwiched between undamaged porous matrix $\mathcal{B}_D$.

3.1 Diffuse interface approximation

This study employs a diffuse approximation for the sharp interface Γ^* by introducing a phase field variable $d \in [0,1]$ which varies smoothly from 0 in $\mathcal{B}_D$ to 1 in $\mathcal{B}_S$. Specifically, we approximate the interfacial area A_{Γ^*} as $A_{\Gamma^*_d}$, which can be expressed in terms of volume integration of surface density functional $\Gamma^*_d(d, \nabla d)$ over $\mathcal{B} = \overline{\mathcal{B}_D \cup \mathcal{B}_S}$ [Miehe et al., 2010, Borden et al., 2012, Suh and Sun, 2019, Suh et al., 2020]:

$$A_{\Gamma^*} \approx A_{\Gamma^*_d} = \int_{\mathcal{B}} \Gamma^*_d(d, \nabla d)\, dV. \tag{22}$$

Here, the size of diffusive zone [i.e., transition zone where $d \in (0,1)$] is controlled by the regularization length scale parameter l^* such that $A_{\Gamma^*_d}$ Γ-converge to A_{Γ^*} [Mumford and Shah, 1989], i.e.,

$$A_{\Gamma^*} = \lim_{l^* \to 0} A_{\Gamma^*_d}. \tag{23}$$

Based on this approach, phase field d and its gradient ∇d can be regarded as smooth approximations of the Heaviside function H_{Γ^*} and the Dirac delta function δ_{Γ^*}, respectively [Stoter et al., 2017, Suh and Sun, 2020]. Therefore, the volume integrals of an arbitrary function $\tilde{G}$ over $\mathcal{B}_D$ and $\mathcal{B}_S$ can respectively be approximated as,

$$\int_{\mathcal{B}_D} \tilde{G}\, dV = \int_{\mathcal{B}} \tilde{G}(1 - H_{\Gamma^*})\, dV = \lim_{l^* \to 0} \int_{\mathcal{B}} \tilde{G}(1-d)\, dV \approx \int_{\mathcal{B}} \tilde{G}(1-d)\, dV, \tag{24}$$

$$\int_{\mathcal{B}_S} \tilde{G}\, dV = \int_{\mathcal{B}} \tilde{G} H_{\Gamma^*}\, dV = \lim_{l^* \to 0} \int_{\mathcal{B}} \tilde{G} d\, dV \approx \int_{\mathcal{B}} \tilde{G} d\, dV. \tag{25}$$

Similarly, the surface integral of the function $\tilde{G}$ along the sharp interface Γ^* can be approximated as,

$$\int_{\Gamma^*} \tilde{G}\, d\Gamma = \int_{\Gamma^*} \tilde{G} \delta_{\Gamma^*}\, dV = \lim_{l^* \to 0} \int_{\mathcal{B}} \tilde{G} \| \nabla d \|\, dV \approx \int_{\mathcal{B}} \tilde{G} \| \nabla d \|\, dV, \tag{26}$$

and we also approximate the normal vector $\boldsymbol{n}^*$ as,

$$\boldsymbol{n}^* \approx -\frac{\nabla d}{\| \nabla d \|}. \tag{27}$$

3.2 Crack growth approximated by evolving phase field

For completeness, this section reviews the phase field model for brittle fracture. We consider the following surface density functional, which is widely used in modeling brittle or quasi-brittle fracture [Bourdin et al., 2008, Miehe et al., 2010, Borden et al., 2012, Bryant and Sun, 2018, Suh et al., 2020] that possesses quadratic local dissipation function:

$$\Gamma^*_d(d, \nabla d) = \frac{d^2}{2l^*} + \frac{l^*}{2}(\nabla d \cdot \nabla d). \tag{28}$$

At this point, we highlight that the evolution of the phase field (i.e., propagation of cavities or cracks) is a mechanical process driven by the effective stress $\boldsymbol{\sigma}'$. In other words, we assume that the solid skeleton is completely damaged in the liquefied zone $\mathcal{B}_S$, whereas in $\mathcal{B}_D$, the solid skeleton remains undamaged. We thus omit the terms that are unrelated to the deformation and fracture in this section. Having critical energy $\mathcal{G}_c$ that is required to create new free surfaces, potential energy density ψ reads,

$$\psi = \underbrace{g(d)\psi_e^+(\boldsymbol{\varepsilon}) + \psi_e^-(\boldsymbol{\varepsilon})}_{\psi_{\text{bulk}}(\boldsymbol{\varepsilon}, d)} + \mathcal{G}_c \Gamma^*_d(d, \nabla d), \tag{29}$$

where $\psi_{\text{bulk}}(\boldsymbol{\varepsilon}, d)$ is the degrading elastic bulk energy and $g(d) = (1-d)^2$ is the degradation function that induces energy dissipation. Following Amor et al. [2009], we adopt additive decomposition scheme that splits the elastic energy ψ_e into compressive (ψ_e^-), and tensile and deviatoric (ψ_e^+) modes, where we

only degrade ψ_e^+ in order to avoid crack propagation under compression [Na and Sun, 2018, Bilgen and Weinberg, 2019, Heider and Sun, 2020], i.e.,

$$\psi_e^+ = \frac{1}{2}K\left\langle \varepsilon^{\mathrm{vol}} \right\rangle_+^2 + \mu(\varepsilon^{\mathrm{dev}} : \varepsilon^{\mathrm{dev}}), \tag{30}$$

$$\psi_e^- = \frac{1}{2}K\left\langle \varepsilon^{\mathrm{vol}} \right\rangle_-^2, \tag{31}$$

where $K = \lambda + 2\mu/3$ is the bulk modulus of the porous matrix, and $\langle \bullet \rangle_\pm = (\bullet \pm |\bullet|)/2$ is the Macaulay bracket operator. In this case, the effective stress tensor σ' can also be decomposed as follows:

$$\sigma' = g(d)\sigma_0'^+ + \sigma_0'^-, \tag{32}$$

where $\sigma_0'^\pm = \partial\psi_e^\pm/\partial\varepsilon$ is the fictitious undamaged effective stress, in which we previously assumed σ_0' to be linear elastic [Eq. (7)].

Based on the fundamental lemma of calculus of variations, the damage evolution equation can be obtained by seeking the stationary point where the functional derivative of Eq. (29) with respect to d vanishes, i.e.,

$$\frac{\partial\psi}{\partial d} - \nabla\cdot\frac{\partial\psi}{\partial\nabla d} = 0, \tag{33}$$

where:

$$\frac{\partial\psi}{\partial d} = g'(d)\psi_e^+ + \frac{\mathcal{G}_c}{l^*}d \ ; \ \nabla\cdot\frac{\partial\psi}{\partial\nabla d} = \mathcal{G}_c l^*\nabla^2 d. \tag{34}$$

Here, the superposed prime denotes derivative with respect to d and $\nabla^2(\bullet) = \nabla\cdot\nabla(\bullet)$ is the Laplacian operator. Furthermore, by following the treatment used in Miehe et al. [2010], we introduce a history function $\mathcal{H}$ which is the pseudo-temporal maximum of the positive energy density (ψ_e^+) in order to ensure crack irreversibility constraint:

$$\mathcal{H} = \max_{\tau\in[0,t]} \psi_e^+. \tag{35}$$

By replacing ψ_e^+ in Eq. (34) with $\mathcal{H}$, Eq. (33) finally yields the following phase field equation that governs the evolution of the interface:

$$g'(d)\mathcal{H} + \frac{\mathcal{G}_c}{l^*}(d - l^{*2}\nabla^2 d) = 0 \text{ in } \mathcal{B}. \tag{36}$$

Note that we can obtain the diffuse representation of the interface by solving Eq. (36), as shown in Fig. 2.

In this study, we leverage the phase field not only as an indicator function for the location of cracks but also for other defects such as cavities or geometrically complicated voids that does not fit for computational homogenization. This approach may efficiently couple the Stokes flow inside the vugs ($\mathcal{B}_S$) that interact with pore fluid in the intact porous matrix ($\mathcal{B}_D$) while both regions are evolving due to the crack growth. A major advantage of this work is that free flow inside the fracture is explicitly replicated and hence there is no need to introduce permeability enhancement models (e.g., cubic law) [Witherspoon et al., 1980, Konzuk and Kueper, 2004, Jin and Arson, 2020]. This explicit treatment enables the simulations to remain physical even in the situations (e.g., high Reynolds number, rough surface, aperture variation) where the validity of the cubic law is questioned [Witherspoon et al., 1980, Miehe and Mauthe, 2016, Heider and Markert, 2017, Wang and Sun, 2017, Sun et al., 2017, Choo and Sun, 2018, Chukwudozie et al., 2019, Wang and Sun, 2019].

Verification and experimental validation of the phase field fracture model for brittle solid has been well documented in the literature. For brevity, similar studies are not provided in this paper. Interested readers may refer to, for instance, such as Nguyen et al. [2016] and Pham et al. [2017].

3.3 Variational formulation of the phase field Biot-Stokes model

We present a immersed phase field Biot-Stokes model designed to simulate the coupled hydro-mechanical behaviors of flow of vuggy porous media with evolving fractures in the brittle regime. This section omits the gravitational effects for brevity (i.e., $\boldsymbol{g} = \boldsymbol{0}$).

The model problem with the sharp interface (Section 2) in which the system possesses two distinct boundaries $\partial\mathcal{B}_D$ and $\partial\mathcal{B}_S$ that can both be decomposed into Dirichlet ($\partial\mathcal{B}_D^u$, $\partial\mathcal{B}_D^p$, $\partial\mathcal{B}_S^w$ and $\partial\mathcal{B}_S^p$) and Neumann ($\partial\mathcal{B}_D^t$, $\partial\mathcal{B}_D^q$, $\partial\mathcal{B}_S^t$ and $\partial\mathcal{B}_S^q$) boundaries satisfying,

$$\partial\mathcal{B}_D = \overline{\partial\mathcal{B}_D^u \cup \partial\mathcal{B}_D^t} = \overline{\partial\mathcal{B}_D^p \cup \partial\mathcal{B}_D^q} \;;\; \emptyset = \partial\mathcal{B}_D^u \cap \partial\mathcal{B}_D^t = \partial\mathcal{B}_D^p \cap \partial\mathcal{B}_D^q, \tag{37}$$

$$\partial\mathcal{B}_S = \overline{\partial\mathcal{B}_S^w \cup \partial\mathcal{B}_S^t} = \overline{\partial\mathcal{B}_S^p \cup \partial\mathcal{B}_S^q} \;;\; \emptyset = \partial\mathcal{B}_S^w \cap \partial\mathcal{B}_S^t = \partial\mathcal{B}_S^p \cap \partial\mathcal{B}_S^q, \tag{38}$$

where the union of $\mathcal{B}_S$ and $\mathcal{B}_D$ is $\mathcal{B}$ and the boundary domain follows the same treatment. Here we capture the transition of the constitutive responses of the solid constituent in the intact and liquefied states through a partition of unity argument in the local constitutive responses. As such, we adopt only one solid constituent and the balance of linear momentum equations in the sub-domains $\mathcal{B}_D$ and $\mathcal{B}_S$ [Eqs (5) and (11)] are combined into one set of equations over the domains $\mathcal{B}$. The governing equations for the model problem are summarized as follows:

$$\begin{cases} (1-d)\left[\nabla\cdot(\boldsymbol{\sigma}' - p_{f_D}\boldsymbol{I})\right] + d\,(\nabla\cdot\boldsymbol{\sigma}^s) = \boldsymbol{0} \text{ in } \mathcal{B}, & (39)\\ \nabla\cdot\boldsymbol{v}_s + \nabla\cdot\boldsymbol{w}_{f_D} = 0 \text{ in } \mathcal{B}_D, & (40)\\ \nabla\cdot\boldsymbol{\sigma}^{f_S} + \rho^{f_S}\boldsymbol{g} = \boldsymbol{0} \text{ in } \mathcal{B}_S, & (41)\\ \nabla\cdot\boldsymbol{v}_s + \nabla\cdot\boldsymbol{w}_{f_S} = 0 \text{ in } \mathcal{B}_S, & (42)\\ g'(d)\mathcal{H} + \dfrac{\mathcal{G}_c}{l^*}(d - l^{*2}\nabla^2 d) = 0 \text{ in } \mathcal{B}, & (43)\\ (\boldsymbol{w}_{f_S} - \boldsymbol{w}_{f_D})\cdot\boldsymbol{n}^* = 0 \text{ on } \Gamma^*, & (44)\\ \boldsymbol{t}^*_{f_S}\cdot\boldsymbol{n}^* + p_{f_D} = 0 \text{ on } \Gamma^*, & (45)\\ \boldsymbol{t}^*_{f_S}\cdot\boldsymbol{m}^*_j + \mu_f\dfrac{\alpha_{SD}}{\sqrt{k}}(\boldsymbol{w}_{f_S} - \boldsymbol{w}_{f_D})\cdot\boldsymbol{m}^*_j = 0 \text{ on } \Gamma^*, & (46) \end{cases}$$

where the natural and essential boundary conditions are not included for brevity. Following the standard weighted residual procedure, we multiply Eqs. (39)-(43) with proper weight functions ($\boldsymbol{\eta}_s$, ξ_{f_D}, $\boldsymbol{\eta}_{f_S}$, ξ_{f_S} and ζ), and integrating over their corresponding domain. The resultant weighted-residual statement reads [Badia et al., 2009, Stoter et al., 2017],

$$\int_{\mathcal{B}} \nabla\boldsymbol{\eta}_s : (\boldsymbol{\sigma}' - p_{f_D}\boldsymbol{I})(1-d)\,dV + \int_{\mathcal{B}} \nabla\boldsymbol{\eta}_s : \boldsymbol{\sigma}^s d\,dV - \int_{\partial\mathcal{B}_D^t} \boldsymbol{\eta}_s\cdot\hat{\boldsymbol{t}}_D\,d\Gamma = 0, \tag{47}$$

$$\int_{\mathcal{B}_D} \xi_{f_D}(\nabla\cdot\dot{\boldsymbol{u}}_s)\,dV - \int_{\mathcal{B}_D} \nabla\xi_{f_D}\cdot\boldsymbol{w}_{f_D}\,dV - \int_{\partial\mathcal{B}_D^q} \xi_{f_D}\hat{q}_D\,d\Gamma + \int_{\Gamma^*} \xi_{f_D}\underbrace{\boldsymbol{w}_{f_D}\cdot(-\boldsymbol{n}^*)}_{=m^*_{f_D}}\,d\Gamma = 0, \tag{48}$$

$$\int_{\mathcal{B}_S} \nabla\boldsymbol{\eta}_{f_S} : \boldsymbol{\sigma}^{f_S}\,dV - \int_{\partial\mathcal{B}_S^t} \boldsymbol{\eta}_{f_S}\cdot\hat{\boldsymbol{t}}_S\,d\Gamma - \int_{\Gamma^*} \boldsymbol{\eta}_{f_S}\cdot\underbrace{\boldsymbol{\sigma}^{f_S}\cdot\boldsymbol{n}^*}_{=\boldsymbol{t}^*_{f_S}}\,d\Gamma = 0, \tag{49}$$

$$\int_{\mathcal{B}_S} \xi_{f_S}(\nabla\cdot\dot{\boldsymbol{u}}_s)\,dV + \int_{\mathcal{B}_S} \xi_{f_S}(\nabla\cdot\boldsymbol{w}_{f_S})\,dV = 0, \tag{50}$$

$$\int_{\mathcal{B}} \zeta\left[g'(d)\mathcal{H} + \frac{\mathcal{G}_c}{l^*}d\right]dV + \int_{\mathcal{B}} \nabla\zeta\cdot\mathcal{G}_c l^*\,\nabla d\,dV = 0, \tag{51}$$

where $\hat{\boldsymbol{t}}_D$ and $\hat{q}_D$ is the prescribed traction and flux at the porous matrix, respectively; and $\hat{\boldsymbol{t}}_S$ is the fluid traction. Then, we directly impose the interfacial transmissibility conditions [Eqs. (44)-(46)] into the field

equations Eqs. (48) and (50). Due to the fluid mass continuity (i.e., $m^*_{f_D} + m^*_{f_S} = 0$), the fourth term on the left hand side of Eq. (48) becomes:

$$\int_{\Gamma^*} \xi_{f_D} \boldsymbol{w}_{f_D} \cdot (-\boldsymbol{n}^*)\, d\Gamma = -\int_{\Gamma^*} \xi_{f_D} \boldsymbol{w}_{f_S} \cdot \boldsymbol{n}^*\, d\Gamma, \tag{52}$$

while normal and shear force equilibrium (i.e., $\boldsymbol{t}^*_{f_D} + \boldsymbol{t}^*_{f_S} = \boldsymbol{0}$) can be imposed at the third term on the left hand side of Eq. (49), i.e.,

$$-\int_{\Gamma^*} \boldsymbol{\eta}_{f_S} \cdot \boldsymbol{\sigma}^{f_S} \cdot \boldsymbol{n}^*\, d\Gamma = \int_{\Gamma^*} \boldsymbol{\eta}_{f_S} \cdot (p_{f_D} \boldsymbol{n}^*)\, d\Gamma + \sum_{j=1}^{2} \int_{\Gamma^*} \boldsymbol{\eta}_{f_S} \cdot \left[\mu_f \frac{\alpha_{SD}}{\sqrt{k}} (\boldsymbol{w}_{f_S} - \boldsymbol{w}_{f_D}) \cdot \boldsymbol{m}^*_j \right] \boldsymbol{m}^*_j\, d\Gamma. \tag{53}$$

Finally, we apply Eqs. (24)-(27) in order to convert subdomain integrals ($\mathcal{B}_D$ and $\mathcal{B}_S$) into integral over the entire domain ($\mathcal{B}$), and to also transform the interface equations [Eqs. (52)-(53)] into a set of immersed boundary conditions. As a result, we get the weak statements for a phase field Biot-Stokes model, which is to: find $\{\boldsymbol{u}_s, p_{f_D}, \boldsymbol{w}_{f_S}, p_{f_S}, d\}$ such that for all $\{\boldsymbol{\eta}_s, \xi_{f_D}, \boldsymbol{\eta}_{f_S}, \xi_{f_S}, \zeta\}$,

$$G^u = G^p_D = G^w_S = G^p_S = G^d = 0, \tag{54}$$

where:

$$G_u = \int_{\mathcal{B}} \nabla \boldsymbol{\eta}_s : (\boldsymbol{\sigma}' - p_{f_D} \boldsymbol{I})(1-d)\, dV + \int_{\mathcal{B}} \nabla \boldsymbol{\eta}_s : \boldsymbol{\sigma}^s d\, dV - \int_{\partial \mathcal{B}^t_D} \boldsymbol{\eta}_s \cdot \hat{\boldsymbol{t}}_D\, d\Gamma, \tag{55}$$

$$G^p_D = \int_{\mathcal{B}} \xi_{f_D} (\nabla \cdot \dot{\boldsymbol{u}}_s)(1-d)\, dV - \int_{\mathcal{B}} \nabla \xi_{f_D} \cdot \boldsymbol{w}_{f_D} (1-d)\, dV + \int_{\mathcal{B}} \xi_{f_D} (\boldsymbol{w}_{f_S} \cdot \nabla d)\, dV - \int_{\partial \mathcal{B}^q_D} \xi_{f_D} \hat{q}_D\, d\Gamma, \tag{56}$$

$$\begin{aligned} G^w_S = &\int_{\mathcal{B}} \nabla \boldsymbol{\eta}_{f_S} : \boldsymbol{\sigma}^{f_S} d\, dV - \int_{\mathcal{B}} \boldsymbol{\eta}_{f_S} \cdot (p_{f_D} \nabla d)\, dV \\ &+ \sum_{j=1}^{2} \int_{\mathcal{B}} \boldsymbol{\eta}_{f_S} \cdot \left[\mu_f \frac{\alpha_{SD}}{\sqrt{k}} (\boldsymbol{w}_{f_S} - \boldsymbol{w}_{f_D}) \cdot \boldsymbol{m}^*_j \right] \boldsymbol{m}^*_j \| \nabla d \|\, dV - \int_{\partial \mathcal{B}^t_S} \boldsymbol{\eta}_{f_S} \cdot \hat{\boldsymbol{t}}_S\, d\Gamma, \end{aligned} \tag{57}$$

$$G^p_S = \int_{\mathcal{B}} \xi_{f_S} (\nabla \cdot \dot{\boldsymbol{u}}_s) d\, dV + \int_{\mathcal{B}} \xi_{f_S} (\nabla \cdot \boldsymbol{w}_{f_S}) d\, dV, \tag{58}$$

$$G^d = \int_{\mathcal{B}} \zeta \left[g'(d) \mathcal{H} + \frac{\mathcal{G}_c}{l^*} d \right] dV + \int_{\mathcal{B}} \nabla \zeta \cdot \mathcal{G}_c l^* \nabla d\, dV. \tag{59}$$

Here, as pointed out in Stoter et al. [2017], the Γ-convergence ensures that the immersed boundary conditions imposed in Eqs. (56)-(57) are consistent with the interface conditions [Eqs. (44)-(46)] if $l^* \to 0$, which in turn confirms the mass conservation and force equilibrium for the entire system $\mathcal{B}$.

4 Numerical examples

This section highlights the capacities of the immersed phase field model to capture the hydromechanical interactions among the pore fluid in the cavities, cracks and the homogenized pore space and the host matrix in two numerical experiments. Our focus is on modeling the problems that involve the mechanically-driven pore fluid migration due to deformation and crack growth inside the solid skeleton. The first example simulates the consolidation process of the porous material that contains a semi-circular cavity at the bottom that serves as a pore fluid outlet, while the second problem showcases the fracture-induced Stokes-Darcy flow in vuggy porous medium.

In order to solve Eqs. (55)-(59) numerically, we adopt standard finite element method where the solution procedure is based on the operator-split [Miehe et al., 2010, Heister et al., 2015, Suh et al., 2020] that successively updates the field variables. In other words, the phase field d is updated first by solving $G^d = 0$, while all other field variables are held fixed, and the solver then advances the remaining variables by solving $\{G^u, G^p_D, G^w_S, G^p_S\}^{\mathrm{T}} = \boldsymbol{0}$. The implementation of our proposed model including finite element discretization and the solution scheme relies on the finite element package `FEniCS` [Logg et al., 2012a,b, Alnæs et al., 2015]. It is noted that there exists multiple different strategies to solve the same system of equations. Since the exploration of different solution schemes are out of the scope of this study, we omit the details for the implementation for brevity.

4.1 Consolidation of porous matrix with a semi-circular cavity

We first simulate a consolidation problem, which has always been one of the key problems in geotechnical engineering. While classical consolidation problem considers time-dependent water expulsion from the homogeneous porous material, as illustrated in Fig. 3, this numerical example explores the case where the system includes a cavity at the bottom that serves as a pore fluid outlet. This specific setting is designed to simulate mechanically driven Stokes-Darcy flow without significant changes in microstructural attributes.

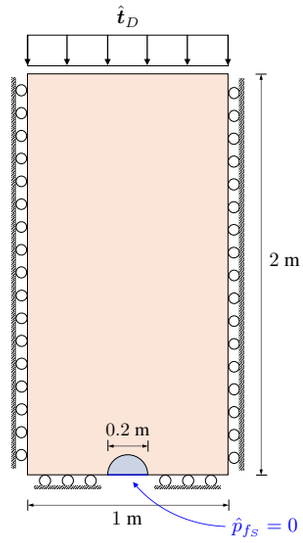

Fig. 3: Schematic of geometry and boundary conditions for the consolidation problem.

The problem domain is a water-saturated 1 m $\times$ 2 m sized rectangular porous matrix ($\mathcal{B}_D$) that contains a semi-circular cavity ($\mathcal{B}_S$) whose diameter is 0.2 m. We prescribe a 1 kPa compressive mechanical traction at the top, while zero pressure boundary is imposed at the bottom of the cavity so that the time-dependent dissipation of pore pressure can be observed. The material parameters for this example are chosen as follows. Intrinsic mass densities for the solid and fluid: $\rho_s = 2700$ kg/m^3 and $\rho_f = 1000$ kg/m^3; Young's modulus and Poisson's ratio of the solid skeleton: $E = 100$ MPa and $\nu = 0.25$; initial permeability and initial porosity of the matrix: $k_0 = 1.0 \times 10^{-8}$ m^2 and $\phi_0 = 0.4$; dynamic viscosity of the fluid phase: $\mu_f = 1.0 \times 10^{-3}$ Pa·sec; slippage coefficient $\alpha_{SD} = 0$; and regularization length for the interface $l^* = 0.002$ m. Furthermore, we assume that solid constituent remains intact in $\mathcal{B}_D$ throughout the simulation while free fluid inside the cavity has zero particle concentration (i.e., $c = 0$).

Fig. 4 shows the spatial distributions for the prime variables at $t = 1.0 \times 10^{-3}$ sec. Here, we compute fluid pressure and relative fluid velocity for the entire system as: $p_f = (1-d)p_{f_D} + dp_{f_S}$ and $\boldsymbol{w}_f = (1-d)\boldsymbol{w}_{f_D} + d\boldsymbol{w}_{f_S}$, respectively, since we have separate degrees of freedoms for pore and free fluids residing in each regions $\mathcal{B}_D$ and $\mathcal{B}_S$. The results imply that applied mechanical load $\hat{\boldsymbol{t}}_D$ at $t = 0$ builds up the pore pressure which in turn affects the pore fluid to migrate towards the cavity. Furthermore, free fluid inside the cavity tends to exhibit higher velocity and lower pressure compared to those of pore fluid, because of different constitutive relations (i.e., Stokes equation and Darcy's law) in each region. As illustrated in Fig. 5, we also investigate the time-dependent response of the system that clearly describes the consolidation process and at the same time highlights the continuous pressure and velocity fields along y-axis (i.e., from the center point of the cavity to the top-central point of the external boundary). At $t = 0$, the entire load is taken by the incompressible pore water which triggers the fluid flow inside the medium. This fluid flow is accompanied by a dissipation of pore pressure over time and an increase in the compression of the entire system, which is consistent with previous studies on homogeneous materials [Li et al., 2004, White and Borja, 2008, Kim et al., 2009, Wang and Sun, 2016]. In addition, the continuous pressure and velocity

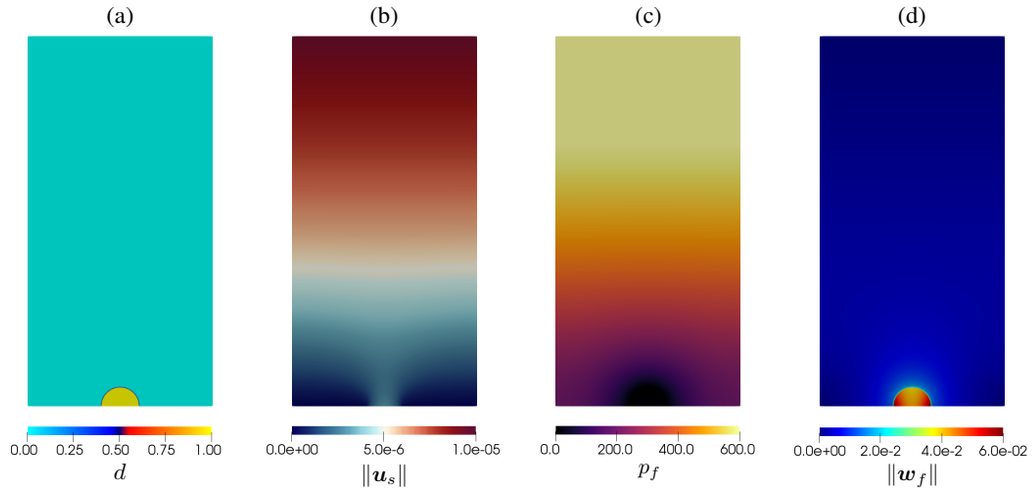

Fig. 4: Spatial distributions of the (a) phase field d; (b) solid displacement $\|\boldsymbol{u}_s\|$ [m]; (c) fluid pressure $p_f = (1-d)p_{f_D} + dp_{f_S}$ [Pa]; and (d) relative fluid velocity $\|\boldsymbol{w}_f\| = \|(1-d)\boldsymbol{w}_{f_D} + d\boldsymbol{w}_{f_S}\|$ [m/s], at $t = 1.0 \times 10^{-3}$ sec.

profiles imply that our model is capable of imposing mass continuity and force equilibrium at the interface as a set of immersed boundary conditions, which confirms the validity of the model.

4.2 Comparison studies on fracture-induced flow in vuggy porous media

In the second set of experiment, we conduct numerical simulations within two different types of domains that possess horizontal edge crack (Fig. 6): one explicitly captures the geometry of the large cavities in the porous media; another one captures the influence of the cavities by increasing the porosity of the homogenized effective medium. While the former approach adopt a more explicit representation of the pore geometry and hence may provide more detailed information on the interactions between the vugs and the propagating cracks, the latter approach could be numerically more efficient. Our objective is to demonstrate, quantitatively, the difference of the two approaches such that a fuller picture on the trade-off between computational efficiency, accuracy and precision of the predictions ca be established.

4.2.1 Modeling vuggy porous media

As illustrated in Fig. 6(a), we first consider a domain that consists of porous matrix with explicitly modeled cavities. Our first representation consists of total nine cavities with different major and minor radii (Table 1) that share the same aspect ratio of 2:1 and are tilted by 45°, such that the volume fraction of the cavities θ_{cav} is 0.056. Here, we assume that the solid skeleton inside the cavities are completely damaged (i.e., $d = 1$), while the porous matrix initially remains completely undamaged (i.e., $d = 0$). The material properties for this case is chosen as follows: $\rho_s = 2700$ kg/m^3, $\rho_f = 1000$ kg/m^3, $E = 20$ GPa, $\nu = 0.2$, $k_0 = 1.0 \times 10^{-12}$ m^2, $\mu_f = 1.0 \times 10^{-3}$ Pa·sec, $\alpha_{SD} = 0.1$, $\mathcal{G}_c = 20$ J/m^2, and $l^* = 0.125 \times 10^{-3}$ m. In addition, the initial particle concentration is chosen as $c_0 = 0.6$ and its upper bound as $c_{\max} = 0.7$, in order to mimic the mudflow inside the cracks or cavities [O'Brien and Julien, 1988, Iverson, 1997].

In contrast, our second domain in Fig. 6(b) is a homogenized representation of Fig. 6(a), where all the cavities are considered as a part of matrix pores. In this case, the porosity of the homogenized medium is determined as: $\phi_{\text{hom}} = (1-\theta_{\text{cav}})\phi_0 + \theta_{\text{cav}} = 0.433$. It is noted the correct homogenized effective properties often depend on the geometry of the vugs or inclusions, which can be determined from computed tomographic images or directly obtained from the experiment [Sun et al., 2011a,b, Kim et al., 2016, Lee et al., 2017]. Since the micro-structural attributes are not always available, this study adopts an alternative

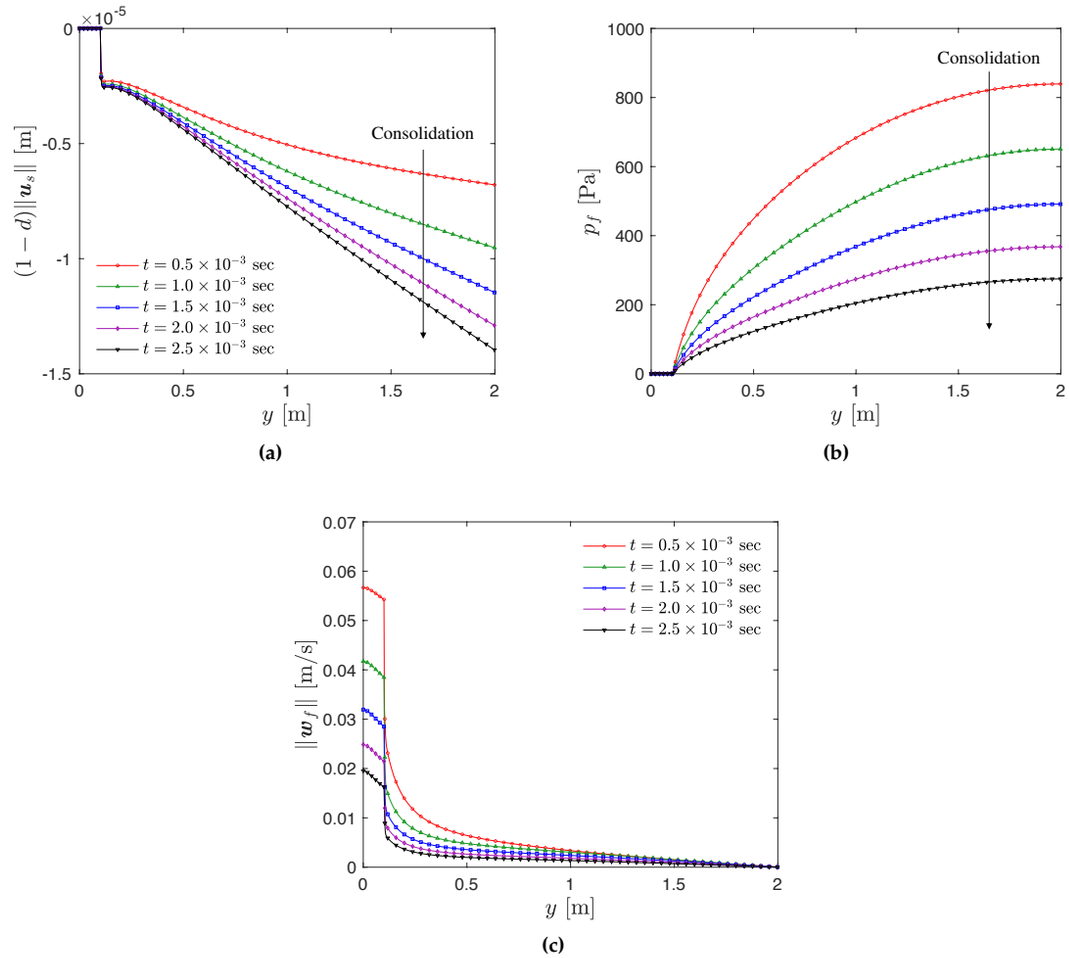

Fig. 5: Response of the saturated Biot-Stokes system under 1 kPa consolidation pressure. (a) Solid displacement; (b) Fluid pressure; and (c) Fluid velocity.

Index	1	2	3	4	5	6	7	8	9
Major radius r_a [mm]	0.400	0.600	0.500	0.500	0.820	0.800	0.580	0.700	0.650
Minor radius r_b [mm]	0.200	0.300	0.250	0.250	0.410	0.400	0.290	0.350	0.325

Table 1: The major and minor radii of the explicitly modeled elliptical cavities in Fig. 6(a).

approach where the effective material properties are determined by using the equivalent inclusion method [Hashin, 1960, Zimmerman, 1991, Ramakrishnan and Arunachalam, 1993]. Following Ramakrishnan and Arunachalam [1993] and by assuming that the matrix shares the same material properties of those chosen for Fig. 6(a), the effective bulk modulus (K_{hom}) and shear modulus (μ_{hom}) for the homogenized representation [Fig. 6(b)] are determined as follows:

$$K_{\text{hom}} = \frac{K(1-\theta_{\text{cav}})^2}{1+\frac{1+\nu}{2(1-2\nu)}\theta_{\text{cav}}} \;;\; \mu_{\text{hom}} = \frac{\mu(1-\theta_{\text{cav}})^2}{1+\frac{11-19\nu}{4(1+\nu)}\theta_{\text{cav}}}, \tag{60}$$

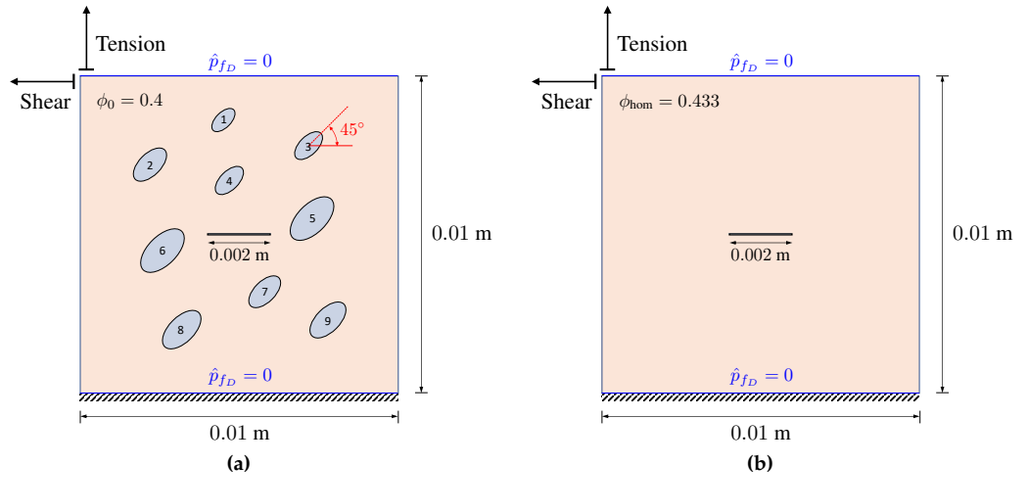

Fig. 6: Schematic of geometry and boundary conditions for the fracture problem. (a) The domain with explicitly modeled cavities; and (b) its homogenized counterpart.

so that the effective Young's modulus $E_{\text{hom}} = 16.50$ GPa and Poisson's ratio $\nu_{\text{hom}} = 0.206$. Assuming that the inclusion permeability is much higher than the matrix permeability, we approximate the effective permeability (k_{hom}) by following Markov et al. [2010] which is obtained based on the Maxwell's formula, i.e.,

$$k_{\text{hom}} = \frac{k_0(1+2\theta_{\text{cav}})}{1-\theta_{\text{cav}}} = 1.18 \times 10^{-12}\ [\text{m}^2]. \tag{61}$$

In addition, since all the cavities in Fig. 6(a) are completely isolated, we adopt the following effective critical energy $\mathcal{G}_{c,\text{hom}}$ proposed by Jelitto and Schneider [2018] for the homogenized representation, which depends on the volume fraction of the cavities, i.e.,

$$\mathcal{G}_{c,\text{hom}} = \mathcal{G}_c(1-\theta_{\text{cav}}^{2/3}) = 17.07\ [\text{J/m}^2]. \tag{62}$$

4.2.2 Mechanically driven fracture-induced flow

As illustrated in Fig. 6, we conduct two different types of simulations within each domain: the tension tests with prescribed vertical displacement rate of 0.01×10^{-3} m/s, and the shear tests with horizontal displacement rate of 0.01×10^{-3} m/s. In both tension and shear tests, the displacements are prescribed at the upper boundary, whereas the bottom part of the domain is held fixed. We also impose hydraulically insulated boundary conditions for the left and right boundaries while we permit water intake from the upper and lower boundaries by imposing $\hat{p}_{f_D} = 0$.

Fig. 7 illustrates the evolution of the phase field for both tension and shear tests in a computational domain where the cavities are explicitly modeled, compared with the crack trajectories obtained from the homogenized domain. The domain without cavities exhibits the crack patterns that are similar to the results of previous studies on homogeneous solids [Miehe et al., 2010, Borden et al., 2012, Bryant and Sun, 2018, Suh et al., 2020], while the domain with explicitly modeled cavities exhibit distinct crack patterns. More importantly, Fig. 8 and Fig. 9 reveals that neglecting the interaction between the cavity and crack in the homogenized model may lead to over-simplified global responses that lacks the distinctive characteristics of the cavity-crack coalescence.

During the numerical experiments, the porous matrix initially undergoes linear elastic deformation until the crack nucleation takes place. At this point, since tensile loading directly influences the volume change of the material, both specimens under tensile load exhibit higher fluid influx at the top, compared to those measured from the shear tests. After the first peaks shown in Fig. 8(a) and Fig. 8(b), cracks start to

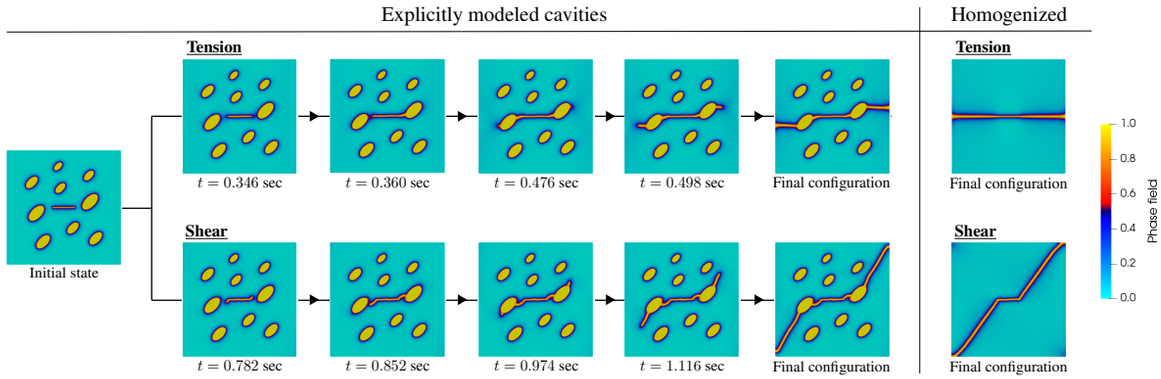

Fig. 7: Evolution of the phase field of the specimens subjected to the numerical tension and shear tests.

initiate from the tips of the pre-existing flaw since they experience higher stress concentration compared to the matrix-cavity interface.

In both tensile and shear experiments performed on the vuggy specimen, the crack nucleation increases the surface influx rate at the permeable boundaries as pore fluid starts to leak from the intact matrix to the damaged regions regardless of the spatial homogenization. The two numerical specimens, nevertheless, begin to behave differently when the cracks propagate towards the adjacent vugs and coalesce with each other in both tension and shear tests in the vuggy specimen (Fig. 7) [Qinami et al., 2019, Suh and Sun, 2020]. These changes in surface influx cannot be replicated in the homogenized porous specimen as the homogenization takes away the possibility of simulating the coalescence between the cavity and the crack.

After the coalescence of the cavity and the crack in the vuggy specimen, the reaction force in both cases increases again with lower influx rates until it reaches the second peak (i.e., where crack nucleation takes place at the matrix-cavity interface), and the crack eventually reaches both end of the specimens. This result implies that the existence of vugs or cavities has a profound impact on the material behavior that cannot be easily replicated in the homogenized effective medium. Consequently, either a more effective macroscopic theory or a suitable multiscale technique is needed to incorporate the cavity-crack interaction into the predictions.

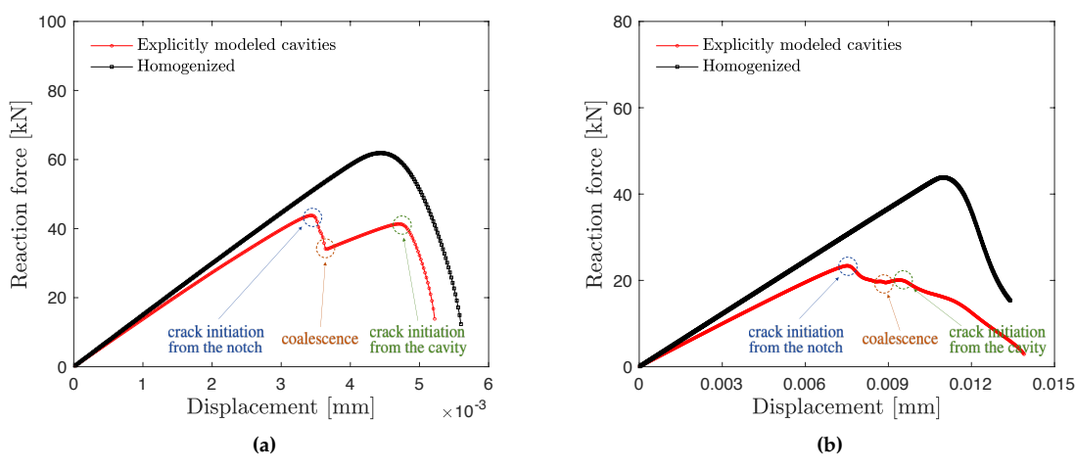

Fig. 8: Force-displacement curves obtained from (a) tension and (b) shear tests.

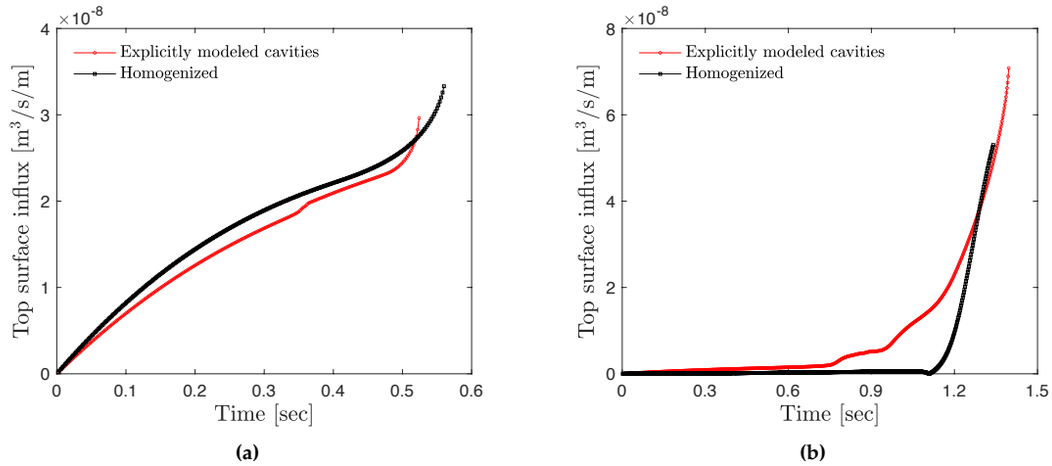

Fig. 9: Fluid influx at the top surface over time measured from (a) tension and (b) shear tests.

Fig. 10 illustrates the pressure (p_f) and x-directional velocity ($\boldsymbol{w}_{f_S}$) fields from a domain with explicitly modeled cavities under tensile and shear loadings, at $t = 0.476$ sec and $t = 1.012$ sec, respectively, where cracks start to propagate from the cavities. Here, the superimposed arrows in Fig. 10 indicate the direction of the velocity vector $\boldsymbol{w}_f = (1-d)\boldsymbol{w}_{f_D} + d\boldsymbol{w}_{f_S}$. In both cases, the leakage of pore fluid takes place towards the interconnected cracks and cavities at the middle, while free fluid in $\mathcal{B}_S$ tends to migrate towards the center, the region where large crack opening displacement occurs. However, it is worthy to note that the fluid flow occurs from the region that has negative pressure to the damaged zone where $p_{f_S} \approx 0$. Unlike previous studies that use the cubic law to predict the hydraulic responses of the flow conduit [Mauthe and Miehe, 2017, Heider and Markert, 2017, Wang and Sun, 2017, Chukwudozie et al., 2019], the pore pressure distribution inside the void space is governed by the Stokes equation directly. This set of numerical experiments again highlight that our proposed model is capable of simulating fracture-cavity interaction with evolving interface, which may not be easily captured either by using hydraulic phase field fracture models or by adopting classical Biot-Stokes model with sharp interface.

To assess the computational efficiency of the proposed model, we record the CPU time for both simulations. A laptop with a Intel Core i9-9880H Processor CPU with 16 GB memory at 2667MHz (DDR4) is used to run both simulation on a single core. Both simulations are solved by the same Scalable Nonlinear Equation Solver (SNES) available in FEniCS. In the case where vuggy pores are explicitly modeled, the time taken to assemble the system of equation is 1.13 second and the averaged time taken to advance one time step with (on average) 5 Newton-Raphson iteration is 35.69 seconds. Meanwhile, in the homogenized case, it takes 1.17 second to assemble the system of equation and 33.34 seconds to advance one time step with also (on average) 5 Newton-Raphson iteration. In general, simulations with the explicitly captured vuggy pores require about 7% more CPU time to run the same simulation.

Future work may consider flow with higher Reynold's number suitable for the Navier-Stokes equation in the fluid domain. Such an extension is nevertheless out of the scope of the current study.

5 Conclusion

This article presents a new immersed phase field model that captures the hydro-mechanical coupling mechanisms in vuggy porous media where brittle cracks filled with water may coalescence with pores that trigger both redistribution of flow and macroscopic softening that cannot be captured without the Stokes-Darcy flow. By generalizing the phase field as an indicator of defects, we introduce a simple and unified treatment to handle the evolving geometries due to crack growths and the resultant changes of constitutive responses without the need of re-meshing or introduction of enrichment functions. By directly

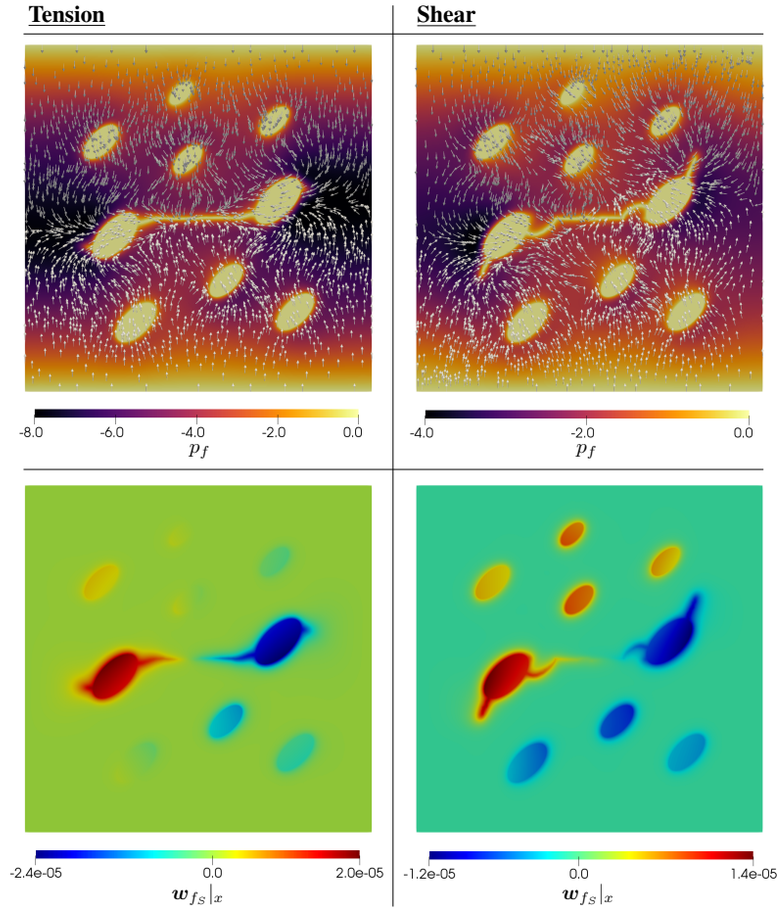

Fig. 10: Snapshots of the pressure $p_f = (1-d)p_{f_D} + dp_{f_S}$ [Pa] and velocity $\boldsymbol{w}_{f_S}$ [m/s] fields obtained from the tension ($t = 0.476$ sec) and shear ($t = 1.012$ sec) tests.

simulating the flow inside the cracks, we bypass the need of introducing phenomenological permeability enhancement model to replicate the flow conduit. This explicit approach can be advantageous over the embedded discontinuity approach when there is a substantial crack opening and a flow near the locations with void-crack interaction where a homogenized pore pressure jump would not be sufficient to capture the pattern of the pore pressure field in the defects. Future work may include the extension of the proposed model to three-dimensional cases as well as extending the Stokes-Darcy flow model for the generalized Navier-Stokes-Darcy flow for injection and other problems with higher Reynolds numbers.

6 Acknowledgments

The suggestions of the two anonymous reviewers are gratefully acknowledged. The authors are thankful for the fruitful discussion with Professor Robert Zimmerman while the second author visited London in 2017. The first author is supported by the Earth Materials and Processes program from the US Army Research Office under grant contract W911NF-18-2-0306. The second author is supported by by the NSF CAREER grant from Mechanics of Materials and Structures program at National Science Foundation under grant contract CMMI-1846875, the Dynamic Materials and Interactions Program from the Air Force Office of Scientific Research under grant contracts FA9550-17-1-0169. These supports are grate- fully acknowledged. The views and conclusions contained in this document are those of the authors, and should not be interpreted as representing the official policies, either expressed or implied, of the sponsors, including the

Army Research Laboratory or the U.S. Government. The U.S. Government is authorized to reproduce and distribute reprints for Government purposes notwithstanding any copyright notation herein.

7 Data availability

The data that support the findings of this study are available from the corresponding author upon request.

References

Martin Alnæs, Jan Blechta, Johan Hake, August Johansson, Benjamin Kehlet, Anders Logg, Chris Richardson, Johannes Ring, Marie E Rognes, and Garth N Wells. The fenics project version 1.5. *Archive of Numerical Software*, 3(100), 2015.

Hanen Amor, Jean-Jacques Marigo, and Corrado Maurini. Regularized formulation of the variational brittle fracture with unilateral contact: Numerical experiments. *Journal of the Mechanics and Physics of Solids*, 57(8):1209–1229, 2009.

Todd Arbogast and Dana S Brunson. A computational method for approximating a darcy–stokes system governing a vuggy porous medium. *Computational geosciences*, 11(3):207–218, 2007.

Todd Arbogast and Heather L Lehr. Homogenization of a darcy–stokes system modeling vuggy porous media. *Computational Geosciences*, 10(3):291–302, 2006.

Chloé Arson and Jean-Michel Pereira. Influence of damage on pore size distribution and permeability of rocks. *International Journal for Numerical and Analytical Methods in Geomechanics*, 37(8):810–831, 2013.

Jean-Louis Auriault. About the beavers and joseph boundary condition. *Transport in porous media*, 83(2): 257–266, 2010.

Santiago Badia, Annalisa Quaini, and Alfio Quarteroni. Coupling biot and navier–stokes equations for modelling fluid–poroelastic media interaction. *Journal of Computational Physics*, 228(21):7986–8014, 2009.

Gordon S Beavers and Daniel D Joseph. Boundary conditions at a naturally permeable wall. *Journal of fluid mechanics*, 30(1):197–207, 1967.

EA Bergkamp, CV Verhoosel, JJC Remmers, and DMJ Smeulders. A staggered finite element procedure for the coupled stokes-biot system with fluid entry resistance. *Computational Geosciences*, pages 1–26, 2020.

James G Berryman and Herbert F Wang. The elastic coefficients of double-porosity models for fluid transport in jointed rock. *Journal of Geophysical Research: Solid Earth*, 100(B12):24611–24627, 1995.

Carola Bilgen and Kerstin Weinberg. On the crack-driving force of phase-field models in linearized and finite elasticity. *Computer Methods in Applied Mechanics and Engineering*, 353:348–372, 2019.

Martin J Blunt, Matthew D Jackson, Mohammad Piri, and Per H Valvatne. Detailed physics, predictive capabilities and macroscopic consequences for pore-network models of multiphase flow. *Advances in Water Resources*, 25(8-12):1069–1089, 2002.

Michael J Borden, Clemens V Verhoosel, Michael A Scott, Thomas JR Hughes, and Chad M Landis. A phase-field description of dynamic brittle fracture. *Computer Methods in Applied Mechanics and Engineering*, 217:77–95, 2012.

Ronaldo I Borja. On the mechanical energy and effective stress in saturated and unsaturated porous continua. *International Journal of Solids and Structures*, 43(6):1764–1786, 2006.

Ronaldo I Borja and Enrique Alarcón. A mathematical framework for finite strain elastoplastic consolidation part 1: Balance laws, variational formulation, and linearization. *Computer Methods in Applied Mechanics and Engineering*, 122(1-2):145–171, 1995.

Blaise Bourdin, Gilles A Francfort, and Jean-Jacques Marigo. The variational approach to fracture. *Journal of elasticity*, 91(1-3):5–148, 2008.

Eric C Bryant and WaiChing Sun. A mixed-mode phase field fracture model in anisotropic rocks with consistent kinematics. *Computer Methods in Applied Mechanics and Engineering*, 342:561–584, 2018.

Robert P Chapuis and Michel Aubertin. On the use of the kozeny carman equation to predict the hydraulic conductivity of soils. *Canadian Geotechnical Journal*, 40(3):616–628, 2003.

Nian-Sheng Cheng and Adrian Wing-Keung Law. Exponential formula for computing effective viscosity. *Powder Technology*, 129(1-3):156–160, 2003.

Jinhyun Choo and Ronaldo I Borja. Stabilized mixed finite elements for deformable porous media with double porosity. *Computer Methods in Applied Mechanics and Engineering*, 293:131–154, 2015.

Jinhyun Choo and WaiChing Sun. Cracking and damage from crystallization in pores: Coupled chemo-hydro-mechanics and phase-field modeling. *Computer Methods in Applied Mechanics and Engineering*, 335: 347–379, 2018.

Jinhyun Choo, Joshua A White, and Ronaldo I Borja. Hydromechanical modeling of unsaturated flow in double porosity media. *International Journal of Geomechanics*, 16(6):D4016002, 2016.

Chukwudi Chukwudozie, Blaise Bourdin, and Keita Yoshioka. A variational phase-field model for hydraulic fracturing in porous media. *Computer Methods in Applied Mechanics and Engineering*, 347:957–982, 2019.

Holger Class, Rainer Helmig, and Peter Bastian. Numerical simulation of non-isothermal multiphase multicomponent processes in porous media.: 1. an efficient solution technique. *Advances in Water Resources*, 25(5):533–550, 2002.

Antonio Costa. Permeability-porosity relationship: A reexamination of the kozeny-carman equation based on a fractal pore-space geometry assumption. *Geophysical research letters*, 33(2), 2006.

Pengcheng Fu, Scott M Johnson, and Charles R Carrigan. An explicitly coupled hydro-geomechanical model for simulating hydraulic fracturing in arbitrary discrete fracture networks. *International Journal for Numerical and Analytical Methods in Geomechanics*, 37(14):2278–2300, 2013.

Jamshid Ghaboussi and Ricardo Barbosa. Three-dimensional discrete element method for granular materials. *International Journal for Numerical and Analytical Methods in Geomechanics*, 14(7):451–472, 1990.

Malcomm Grant. *Geothermal reservoir engineering*. Elsevier, 2013.

Chunsheng Guo, Yanwei Li, Xianbo Nian, Minghai Xu, Hai Liu, and Yaan Wang. Experimental study on the slip velocity of turbulent flow over and within porous media. *Physics of Fluids*, 32(1):015111, 2020.

Zvi Hashin. The elastic moduli of heterogeneous materials. Technical report, HARVARD UNIV CAMBRIDGE MA, 1960.

Y Heider and B Markert. A phase-field modeling approach of hydraulic fracture in saturated porous media. *Mechanics Research Communications*, 80:38–46, 2017.

Yousef Heider and WaiChing Sun. A phase field framework for capillary-induced fracture in unsaturated porous media: Drying-induced vs. hydraulic cracking. *Computer Methods in Applied Mechanics and Engineering*, 359:112647, 2020.

Timo Heister, Mary F Wheeler, and Thomas Wick. A primal-dual active set method and predictor-corrector mesh adaptivity for computing fracture propagation using a phase-field approach. *Computer Methods in Applied Mechanics and Engineering*, 290:466–495, 2015.

Jeffrey D Hyman, Satish Karra, Nataliia Makedonska, Carl W Gable, Scott L Painter, and Hari S Viswanathan. dfnworks: A discrete fracture network framework for modeling subsurface flow and transport. *Computers & Geosciences*, 84:10–19, 2015.

Richard M Iverson. The physics of debris flows. *Reviews of geophysics*, 35(3):245–296, 1997.

John Conrad Jaeger, Neville GW Cook, and Robert Zimmerman. *Fundamentals of rock mechanics*. John Wiley & Sons, 2009.

Hans Jelitto and Gerold A Schneider. A geometric model for the fracture toughness of porous materials. *Acta materialia*, 151:443–453, 2018.

Wencheng Jin and Chloé Arson. Fluid-driven transition from damage to fracture in anisotropic porous media: a multi-scale xfem approach. *Acta Geotechnica*, 15(1):113–144, 2020.

Ruben Juanes, EJ Spiteri, FM Orr Jr, and MJ Blunt. Impact of relative permeability hysteresis on geological co2 storage. *Water resources research*, 42(12), 2006.

Dong Hun Kang, Tae Sup Yun, Kwang Yeom Kim, and Jaewon Jang. Effect of hydrate nucleation mechanisms and capillarity on permeability reduction in granular media. *Geophysical Research Letters*, 43(17): 9018–9025, 2016.

Jihoon Kim, Hamdi A Tchelepi, Ruben Juanes, et al. Stability, accuracy and efficiency of sequential methods for coupled flow and geomechanics. In *SPE reservoir simulation symposium*. Society of Petroleum Engineers, 2009.

Kwang Yeom Kim, Hyoung Suk Suh, Tae Sup Yun, Seong-Woo Moon, and Yong-Seok Seo. Effect of particle shape on the shear strength of fault gouge. *Geosciences Journal*, 20(3):351–359, 2016.

Julie S Konzuk and Bernard H Kueper. Evaluation of cubic law based models describing single-phase flow through a rough-walled fracture. *Water Resources Research*, 40(2), 2004.

PV Lade and R De Boer. The concept of effective stress for soil, concrete and rock. *Geotechnique*, 47(1):61–78, 1997.

William J Layton, Friedhelm Schieweck, and Ivan Yotov. Coupling fluid flow with porous media flow. *SIAM Journal on Numerical Analysis*, 40(6):2195–2218, 2002.

Changho Lee, Hyoung Suk Suh, Boyeong Yoon, and Tae Sup Yun. Particle shape effect on thermal conductivity and shear wave velocity in sands. *Acta Geotechnica*, 12(3):615–625, 2017.

Colin TO Leung and Robert W Zimmerman. Estimating the hydraulic conductivity of two-dimensional fracture networks using network geometric properties. *Transport in porous media*, 93(3):777–797, 2012.

Chao Li, Ronaldo I Borja, and Richard A Regueiro. Dynamics of porous media at finite strain. *Computer methods in applied mechanics and engineering*, 193(36-38):3837–3870, 2004.

Zhilin Li, Ming-Chih Lai, Xiaofei Peng, and Zhiyue Zhang. A least squares augmented immersed interface method for solving navier–stokes and darcy coupling equations. *Computers & Fluids*, 167:384–399, 2018.

Chao Liu and Younane N Abousleiman. Shale dual-porosity dual-permeability poromechanical and chemical properties extracted from experimental pressure transmission tests. *Journal of Engineering Mechanics*, 143(9):04017107, 2017.

Anders Logg, Kent-Andre Mardal, and Garth Wells. *Automated solution of differential equations by the finite element method: The FEniCS book*, volume 84. Springer Science & Business Media, 2012a.

Anders Logg, Garth N Wells, and Johan Hake. Dolfin: A c++/python finite element library. In *Automated solution of differential equations by the finite element method*, pages 173–225. Springer, 2012b.

M Markov, E Kazatchenko, A Mousatov, and E Pervago. Permeability of the fluid-filled inclusions in porous media. *Transport in porous media*, 84(2):307–317, 2010.

S Mauran, L Rigaud, and O Coudevylle. Application of the carman–kozeny correlation to a high-porosity and anisotropic consolidated medium: the compressed expanded natural graphite. *Transport in porous media*, 43(2):355–376, 2001.

Steffen Mauthe and Christian Miehe. Hydraulic fracture in poro-hydro-elastic media. *Mechanics Research Communications*, 80:69–83, 2017.

Gary Mavko and Amos Nur. The effect of a percolation threshold in the kozeny-carman relation. *Geophysics*, 62(5):1480–1482, 1997.

Christian Miehe and Steffen Mauthe. Phase field modeling of fracture in multi-physics problems. part iii. crack driving forces in hydro-poro-elasticity and hydraulic fracturing of fluid-saturated porous media. *Computer Methods in Applied Mechanics and Engineering*, 304:619–655, 2016.

Christian Miehe, Martina Hofacker, and Fabian Welschinger. A phase field model for rate-independent crack propagation: Robust algorithmic implementation based on operator splits. *Computer Methods in Applied Mechanics and Engineering*, 199(45-48):2765–2778, 2010.

Andro Mikelic and Willi Jäger. On the interface boundary condition of beavers, joseph, and saffman. *SIAM Journal on Applied Mathematics*, 60(4):1111–1127, 2000.

Vincent Monchiet, Hai-Bang Ly, and Daniel Grande. Macroscopic permeability of doubly porous materials with cylindrical and spherical macropores. *Meccanica*, 54(10):1583–1596, 2019.

Melvin Mooney. The viscosity of a concentrated suspension of spherical particles. *Journal of colloid science*, 6(2):162–170, 1951.

David Bryant Mumford and Jayant Shah. Optimal approximations by piecewise smooth functions and associated variational problems. *Communications on pure and applied mathematics*, 1989.

SeonHong Na and WaiChing Sun. Computational thermomechanics of crystalline rock, part i: A combined multi-phase-field/crystal plasticity approach for single crystal simulations. *Computer Methods in Applied Mechanics and Engineering*, 338:657–691, 2018.

Thanh Tung Nguyen, Julien Yvonnet, Michel Bornert, Camille Chateau, Karam Sab, R Romani, and Robert Le Roy. On the choice of parameters in the phase field method for simulating crack initiation with experimental validation. *International Journal of Fracture*, 197(2):213–226, 2016.

Jim S O'Brien and Pierre Y Julien. Laboratory analysis of mudflow properties. *Journal of hydraulic engineering*, 114(8):877–887, 1988.

Erdal Ozkan, Rajagopal S Raghavan, Osman Gonul Apaydin, et al. Modeling of fluid transfer from shale matrix to fracture network. In *SPE Annual Technical Conference and Exhibition*. Society of Petroleum Engi-

neers, 2010.

A Paterson and M Fermigier. Wetting of heterogeneous surfaces: Influence of defect interactions. *Physics of Fluids*, 9(8):2210–2216, 1997.

Jean-Michel Pereira and Chloé Arson. Retention and permeability properties of damaged porous rocks. *Computers and Geotechnics*, 48:272–282, 2013.

KH Pham, K Ravi-Chandar, and CM Landis. Experimental validation of a phase-field model for fracture. *International Journal of Fracture*, 205(1):83–101, 2017.

Aurel Qinami, Eric Cushman Bryant, WaiChing Sun, and Michael Kaliske. Circumventing mesh bias by r-and h-adaptive techniques for variational eigenfracture. *International Journal of Fracture*, 220(2):129–142, 2019.

N Ramakrishnan and VS Arunachalam. Effective elastic moduli of porous ceramic materials. *Journal of the American Ceramic Society*, 76(11):2745–2752, 1993.

J Rutqvist, J Birkholzer, F Cappa, and C-F Tsang. Estimating maximum sustainable injection pressure during geological sequestration of co2 using coupled fluid flow and geomechanical fault-slip analysis. *Energy Conversion and Management*, 48(6):1798–1807, 2007.

Philip Geoffrey Saffman. On the boundary condition at the surface of a porous medium. *Studies in applied mathematics*, 50(2):93–101, 1971.

PMTM Schutjens, TH Hanssen, MHH Hettema, J Merour, Ph De Bree, JWA Coremans, G Helliesen, et al. Compaction-induced porosity/permeability reduction in sandstone reservoirs: data and model for elasticity-dominated deformation. *SPE Reservoir Evaluation & Engineering*, 7(03):202–216, 2004.

APS Selvadurai, Cyrille-B Couture, and SM Rezaei Niya. Permeability of wormholes created by co2-acidized water flow through stressed carbonate rocks. *Physics of Fluids*, 29(9):096604, 2017.

Michael AA Spaid and Frederick R Phelan Jr. Lattice boltzmann methods for modeling microscale flow in fibrous porous media. *Physics of fluids*, 9(9):2468–2474, 1997.

Stein KF Stoter, Peter Müller, Luca Cicalese, Massimiliano Tuveri, Dominik Schillinger, and Thomas JR Hughes. A diffuse interface method for the navier–stokes/darcy equations: Perfusion profile for a patient-specific human liver based on mri scans. *Computer Methods in Applied Mechanics and Engineering*, 321:70–102, 2017.

Hyoung Suk Suh and WaiChing Sun. An open-source fenics implementation of a phase field fracture model for micropolar continua. *International Journal for Multiscale Computational Engineering*, 17(6), 2019.

Hyoung Suk Suh and WaiChing Sun. An immersed phase field fracture model for fluid-infiltrating porous media with evolving beavers-joseph-saffman condition. *arXiv preprint arXiv:2008.11815*, 2020.

Hyoung Suk Suh and Tae Sup Yun. Modification of capillary pressure by considering pore throat geometry with the effects of particle shape and packing features on water retention curves for uniformly graded sands. *Computers and Geotechnics*, 95:129–136, 2018.

Hyoung Suk Suh, Dong Hun Kang, Jaewon Jang, Kwang Yeom Kim, and Tae Sup Yun. Capillary pressure at irregularly shaped pore throats: Implications for water retention characteristics. *Advances in Water Resources*, 110:51–58, 2017.

Hyoung Suk Suh, WaiChing Sun, and Devin T. O'Connor. A phase field model for cohesive fracture in micropolar continua. *Computer Methods in Applied Mechanics and Engineering*, 369:113181, 2020. ISSN 0045-7825. doi: https://doi.org/10.1016/j.cma.2020.113181. URL http://www.sciencedirect.com/science/article/pii/S0045782520303662.

Wai Ching Sun, Jose E Andrade, and John W Rudnicki. Multiscale method for characterization of porous microstructures and their impact on macroscopic effective permeability. *International Journal for Numerical Methods in Engineering*, 88(12):1260–1279, 2011a.

WaiChing Sun and Teng-fong Wong. Prediction of permeability and formation factor of sandstone with hybrid lattice boltzmann/finite element simulation on microtomographic images. *International Journal of Rock Mechanics and Mining Sciences*, 106:269–277, 2018.

WaiChing Sun, José E Andrade, John W Rudnicki, and Peter Eichhubl. Connecting microstructural attributes and permeability from 3d tomographic images of in situ shear-enhanced compaction bands using multiscale computations. *Geophysical Research Letters*, 38(10), 2011b.

WaiChing Sun, Jakob T Ostien, and Andrew G Salinger. A stabilized assumed deformation gradient finite element formulation for strongly coupled poromechanical simulations at finite strain. *International Journal for Numerical and Analytical Methods in Geomechanics*, 37(16):2755–2788, 2013.

WaiChing Sun, Zhijun Cai, and Jinhyun Choo. Mixed arlequin method for multiscale poromechanics problems. *International Journal for Numerical Methods in Engineering*, 111(7):624–659, 2017.

GH Tang, WQ Tao, and YL He. Lattice boltzmann method for gaseous microflows using kinetic theory boundary conditions. *Physics of Fluids*, 17(5):058101, 2005.

A Terzis, I Zarikos, K Weishaupt, G Yang, X Chu, R Helmig, and B Weigand. Microscopic velocity field measurements inside a regular porous medium adjacent to a low reynolds number channel flow. *Physics of Fluids*, 31(4):042001, 2019.

Justin L Wagner, Katya M Casper, Steven J Beresh, Patrick S Hunter, Russell W Spillers, John F Henfling, and Randall L Mayes. Fluid-structure interactions in compressible cavity flows. *Physics of Fluids*, 27(6): 066102, 2015.

Kun Wang and WaiChing Sun. A semi-implicit discrete-continuum coupling method for porous media based on the effective stress principle at finite strain. *Computer Methods in Applied Mechanics and Engineering*, 304:546–583, 2016.

Kun Wang and WaiChing Sun. A unified variational eigen-erosion framework for interacting brittle fractures and compaction bands in fluid-infiltrating porous media. *Computer Methods in Applied Mechanics and Engineering*, 318:1–32, 2017.

Kun Wang and WaiChing Sun. A multiscale multi-permeability poroplasticity model linked by recursive homogenizations and deep learning. *Computer Methods in Applied Mechanics and Engineering*, 334:337–380, 2018.

Kun Wang and WaiChing Sun. An updated lagrangian lbm–dem–fem coupling model for dual-permeability fissured porous media with embedded discontinuities. *Computer Methods in Applied Mechanics and Engineering*, 344:276–305, 2019.

Joshua A White and Ronaldo I Borja. Stabilized low-order finite elements for coupled solid-deformation/fluid-diffusion and their application to fault zone transients. *Computer Methods in Applied Mechanics and Engineering*, 197(49-50):4353–4366, 2008.

Paul Adams Witherspoon, Joseph SY Wang, K Iwai, and John E Gale. Validity of cubic law for fluid flow in a deformable rock fracture. *Water resources research*, 16(6):1016–1024, 1980.

Paul F Worthington. The uses and abuses of the archie equations, 1: The formation factor-porosity relationship. *Journal of Applied Geophysics*, 30(3):215–228, 1993.

Zhenxing Wu and Parisa Mirbod. Experimental analysis of the flow near the boundary of random porous media. *Physics of Fluids*, 30(4):047103, 2018.

Robert W Zimmerman. Elastic moduli of a solid containing spherical inclusions. *Mechanics of Materials*, 12 (1):17–24, 1991.

RW Zimmerman. Coupling in poroelasticity and thermoelasticity. *International Journal of Rock Mechanics and Mining Sciences*, 37(1-2):79–87, 2000.

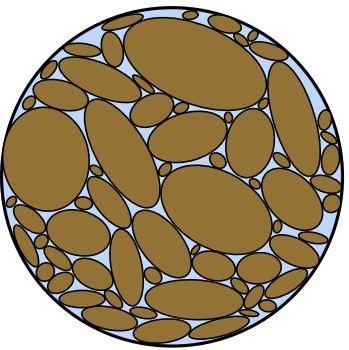

Intact porous matrix

- Solid skeleton
- Pore fluid

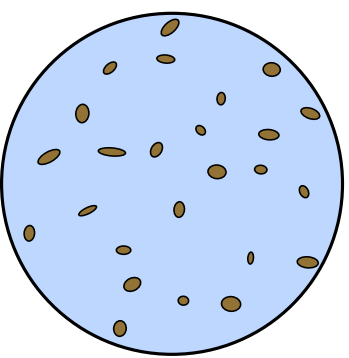

Solid-fluid mixture

- Liquefied solid
- Free fluid

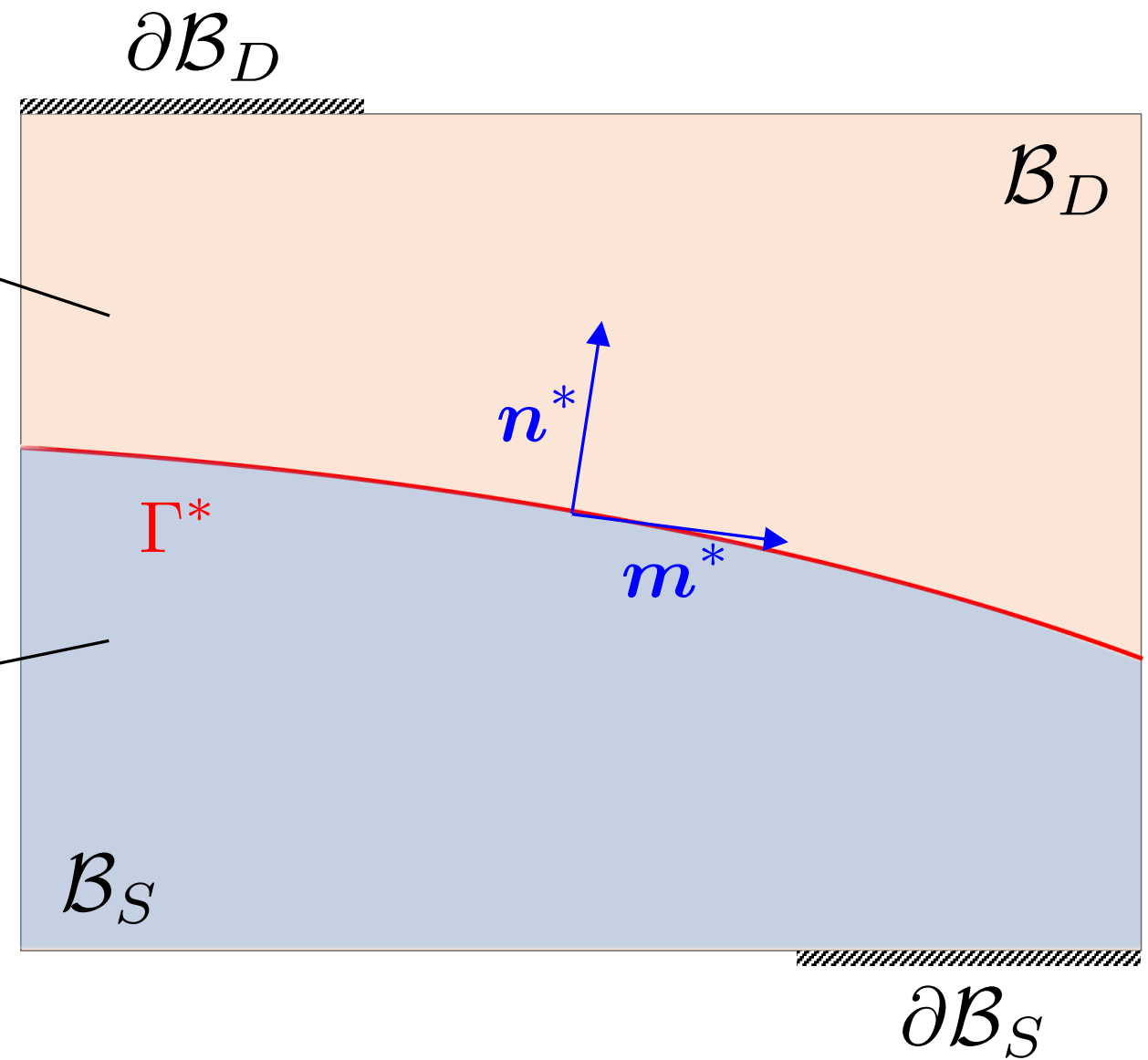

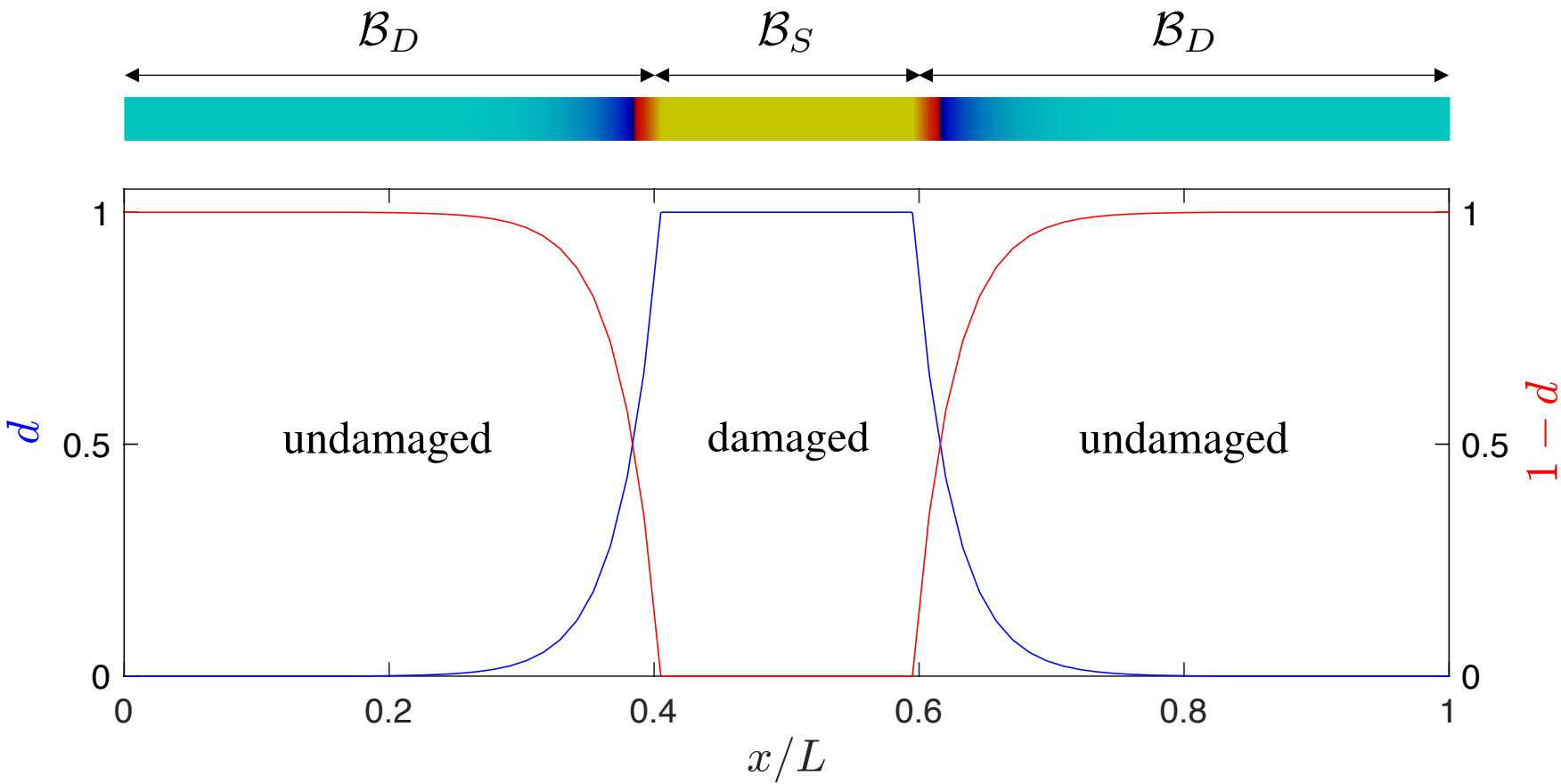
$\mathcal{B}_D$
$\mathcal{B}_S$
$\mathcal{B}_D$
1
0.5
0
d
undamaged
damaged
undamaged
1
0.5
0
$1-d$
0
0.2
0.4
0.6
0.8
1
x/L

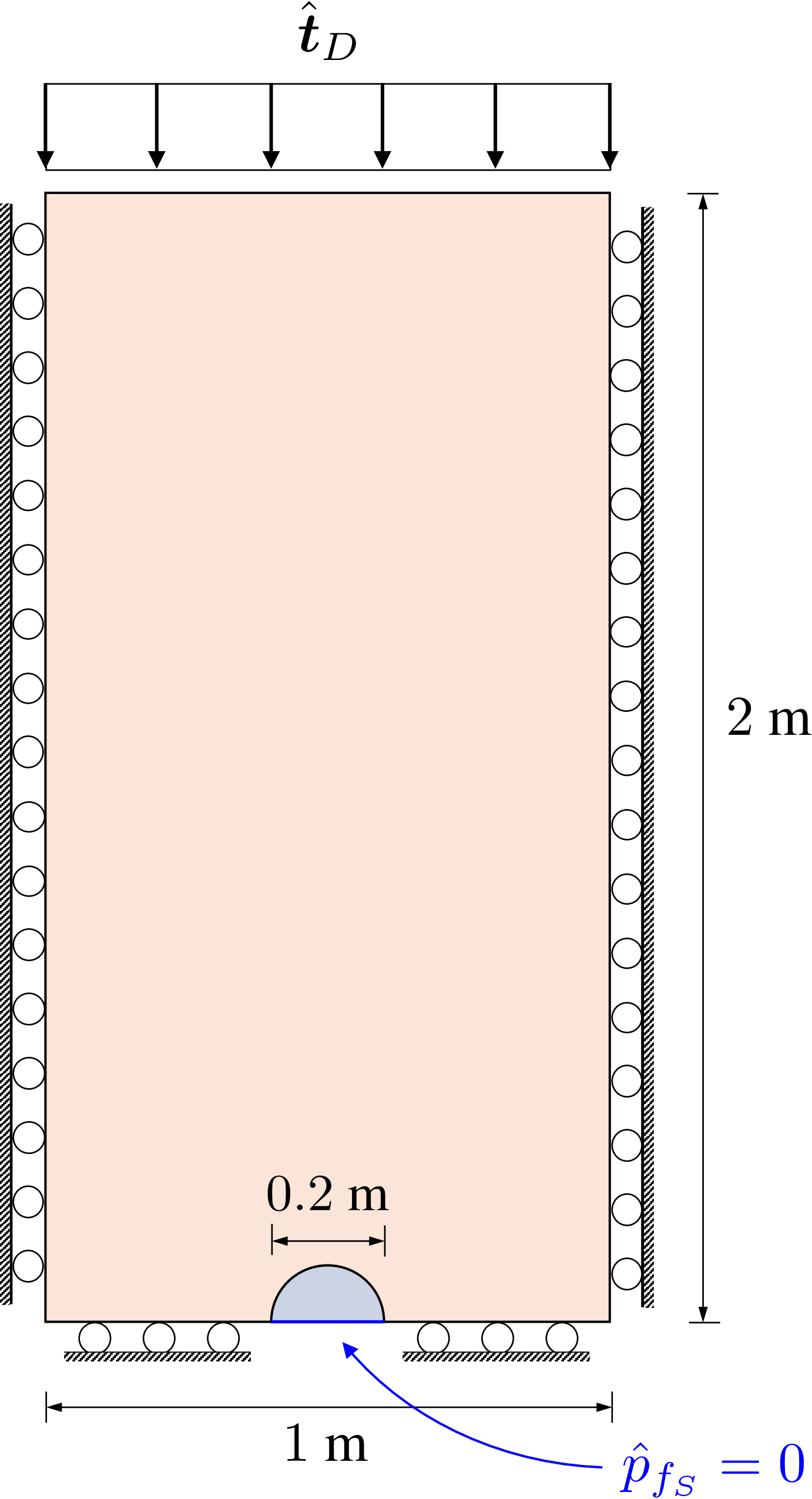
$\hat{\boldsymbol{t}}_D$
2 m
0.2 m
1 m
$\hat{p}_{f_S} = 0$

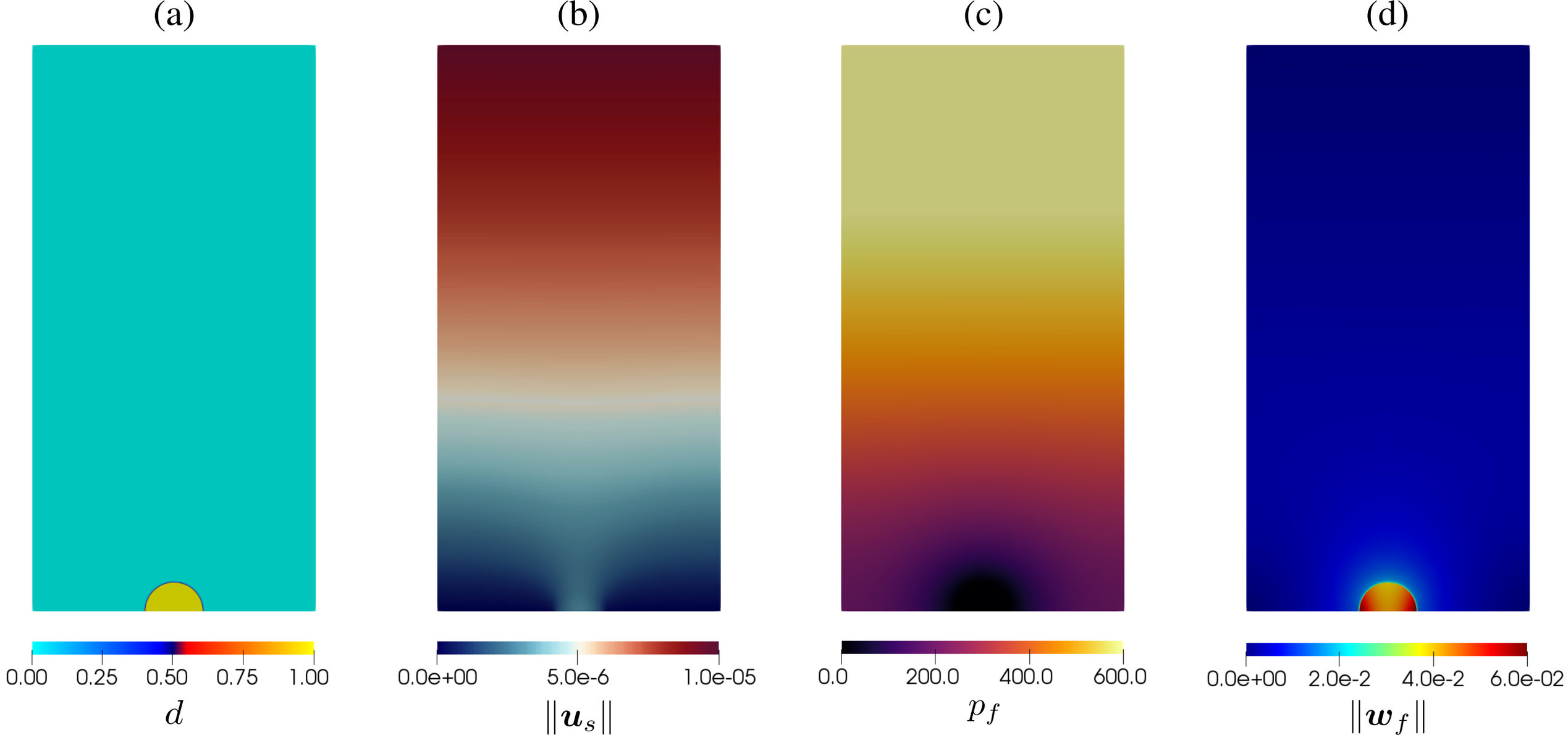
(a)
(b)
(c)
(d)
0.00
0.25
0.50
0.75
1.00
d
0.0e+00
5.0e-6
1.0e-05
$\|\boldsymbol{u}_s\|$
0.0
200.0
400.0
600.0
p_f
0.0e+00
2.0e-2
4.0e-2
6.0e-02
$\|\boldsymbol{w}_f\|$

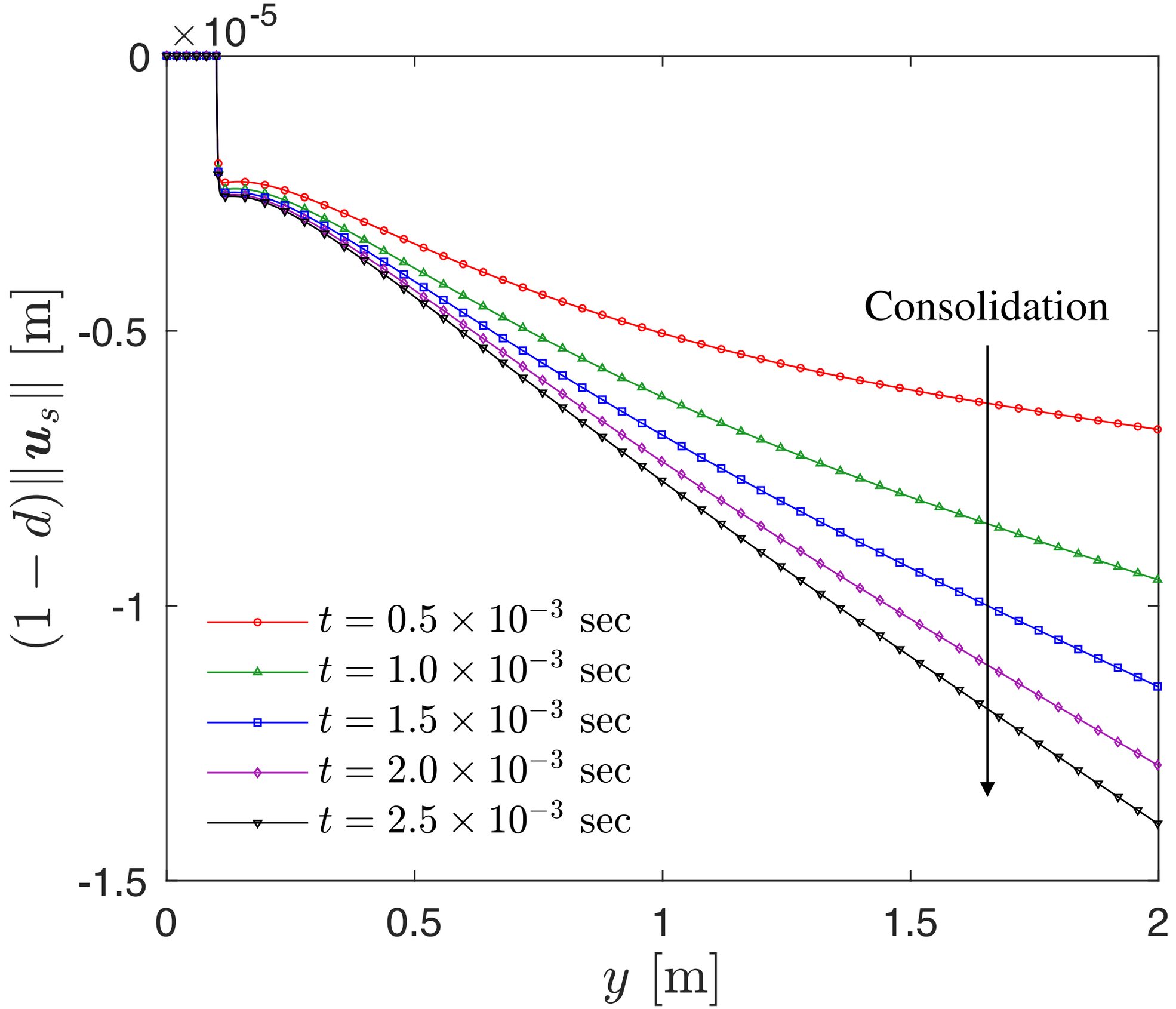
$\times 10^{-5}$
0
-0.5
-1
-1.5
0
0.5
1
1.5
2
$(1-d)\|\boldsymbol{u}_s\|$ [m]
y [m]
Consolidation
$t = 0.5 \times 10^{-3}$ sec
$t = 1.0 \times 10^{-3}$ sec
$t = 1.5 \times 10^{-3}$ sec
$t = 2.0 \times 10^{-3}$ sec
$t = 2.5 \times 10^{-3}$ sec

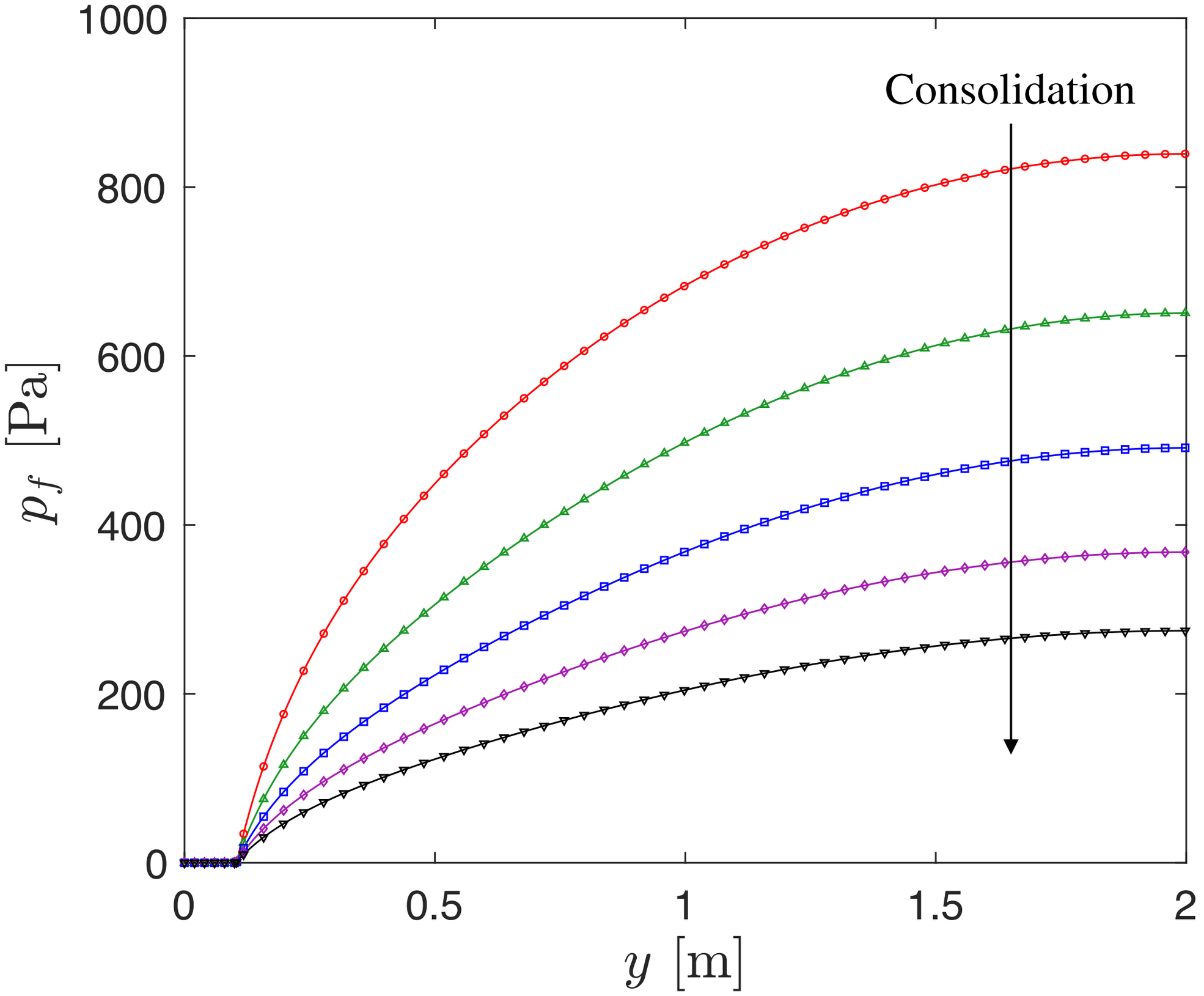
Consolidation
1000
800
600
400
200
0
0
0.5
1
1.5
2
p_f [Pa]
y [m]

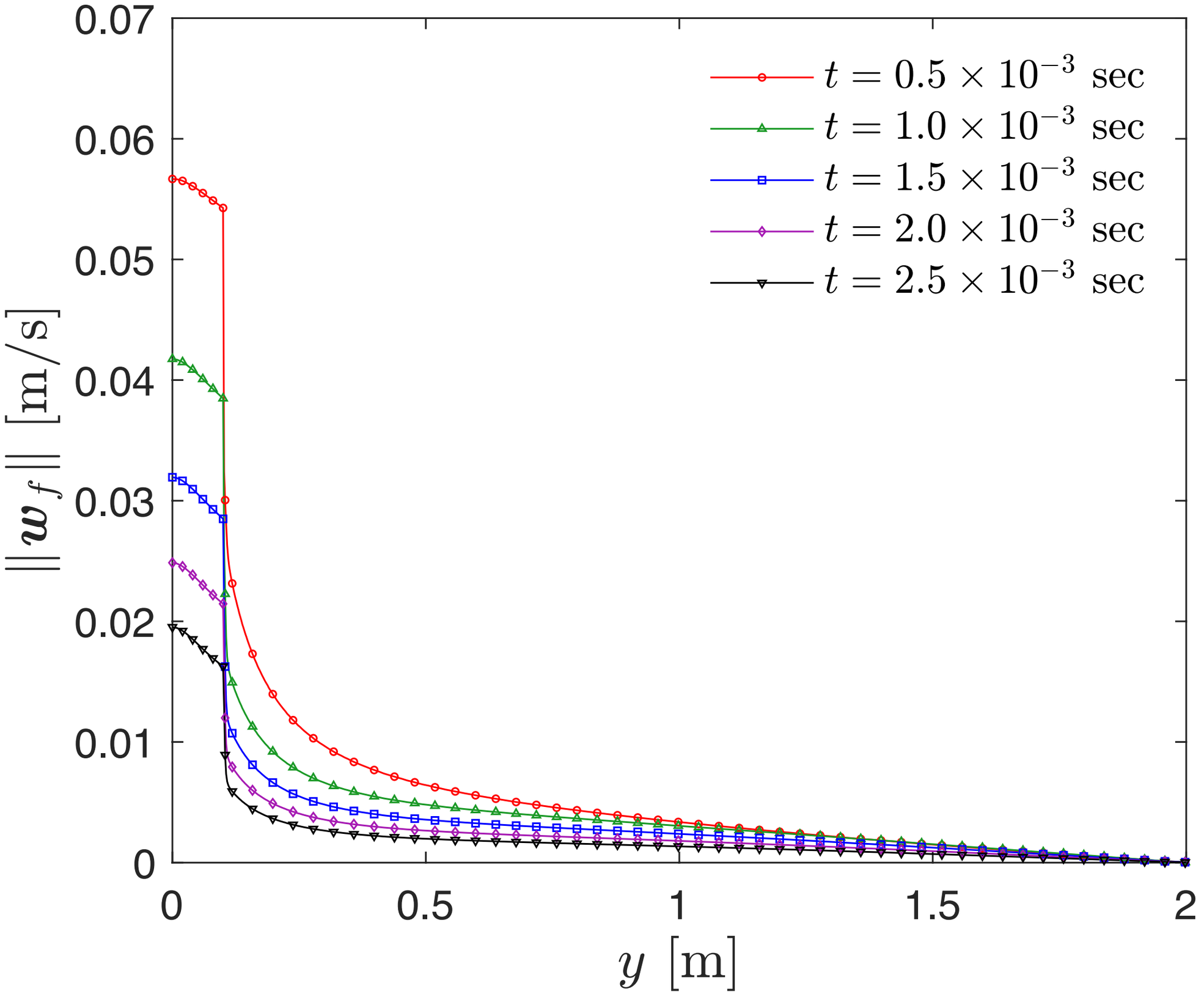
0.07
0.06
0.05
0.04
0.03
0.02
0.01
0
0
0.5
1
1.5
2
$t = 0.5 \times 10^{-3}$ sec
$t = 1.0 \times 10^{-3}$ sec
$t = 1.5 \times 10^{-3}$ sec
$t = 2.0 \times 10^{-3}$ sec
$t = 2.5 \times 10^{-3}$ sec
$\|\boldsymbol{w}_f\|$ [m/s]
y [m]

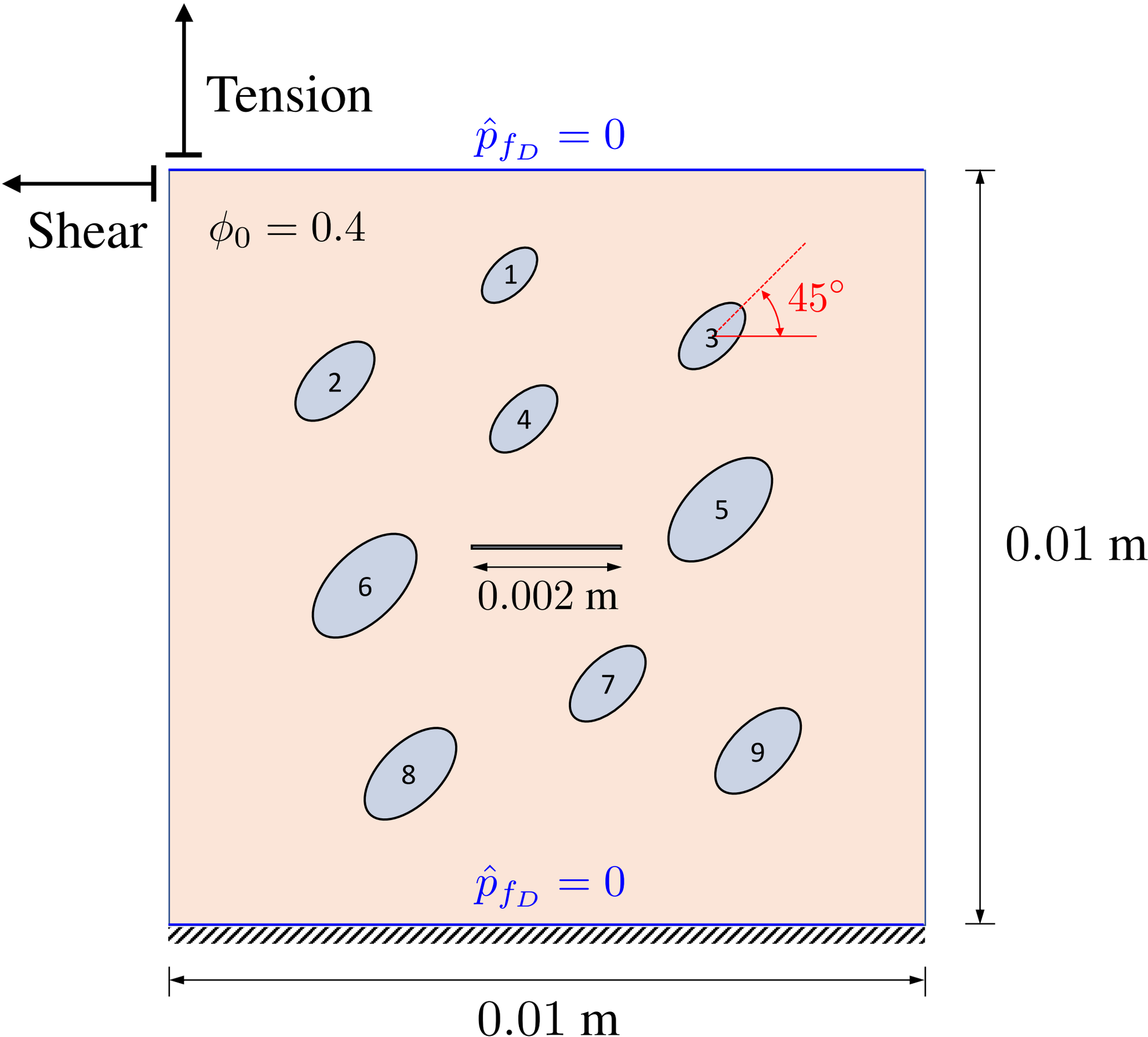
Tension
Shear
$\hat{p}_{f_D} = 0$
$\phi_0 = 0.4$
1
2
3
4
5
6
7
8
9
45°
0.002 m
0.01 m
$\hat{p}_{f_D} = 0$
0.01 m

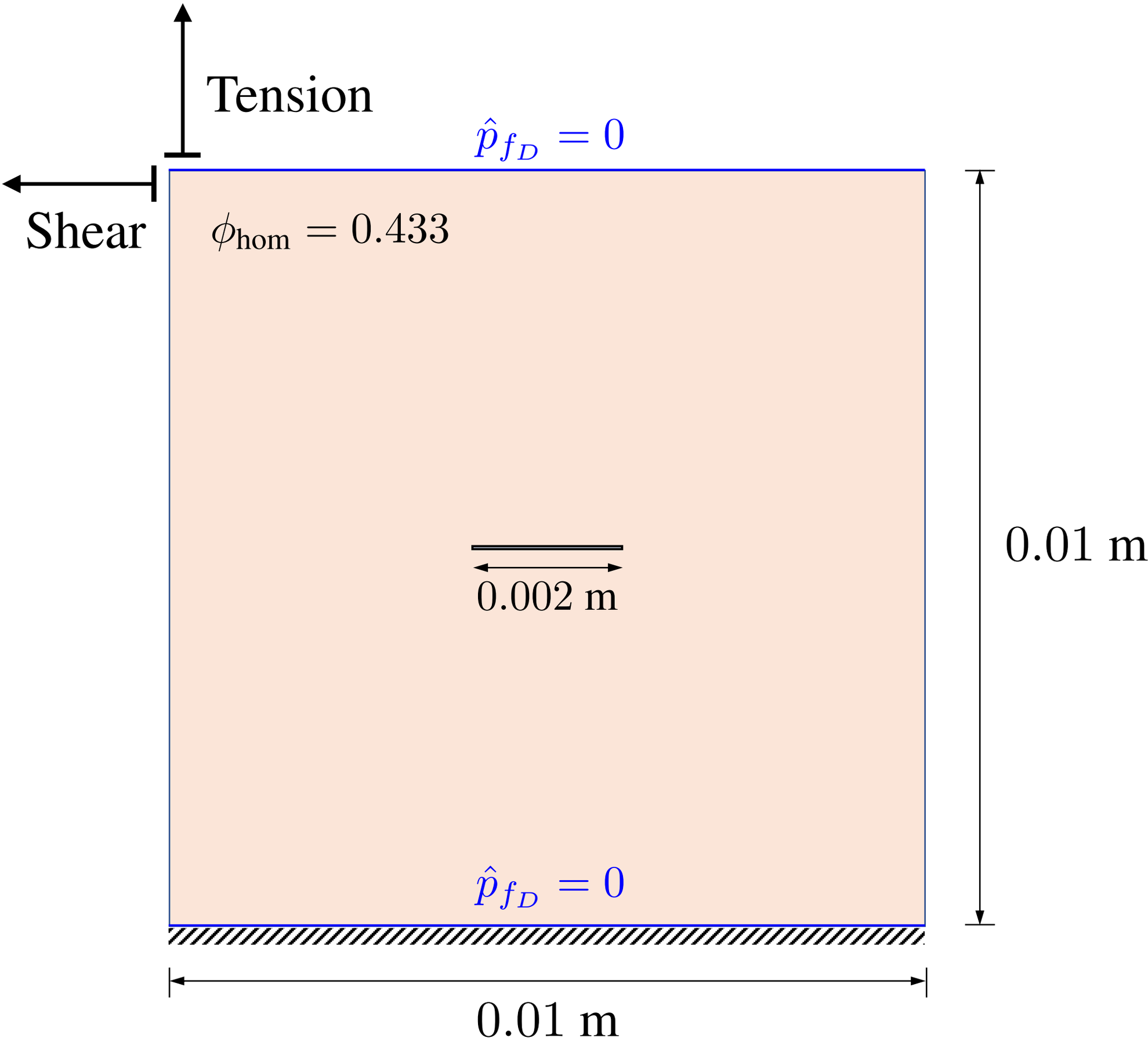
Tension
$\hat{p}_{f_D} = 0$
Shear
$\phi_{\text{hom}} = 0.433$
0.01 m
0.002 m
$\hat{p}_{f_D} = 0$
0.01 m

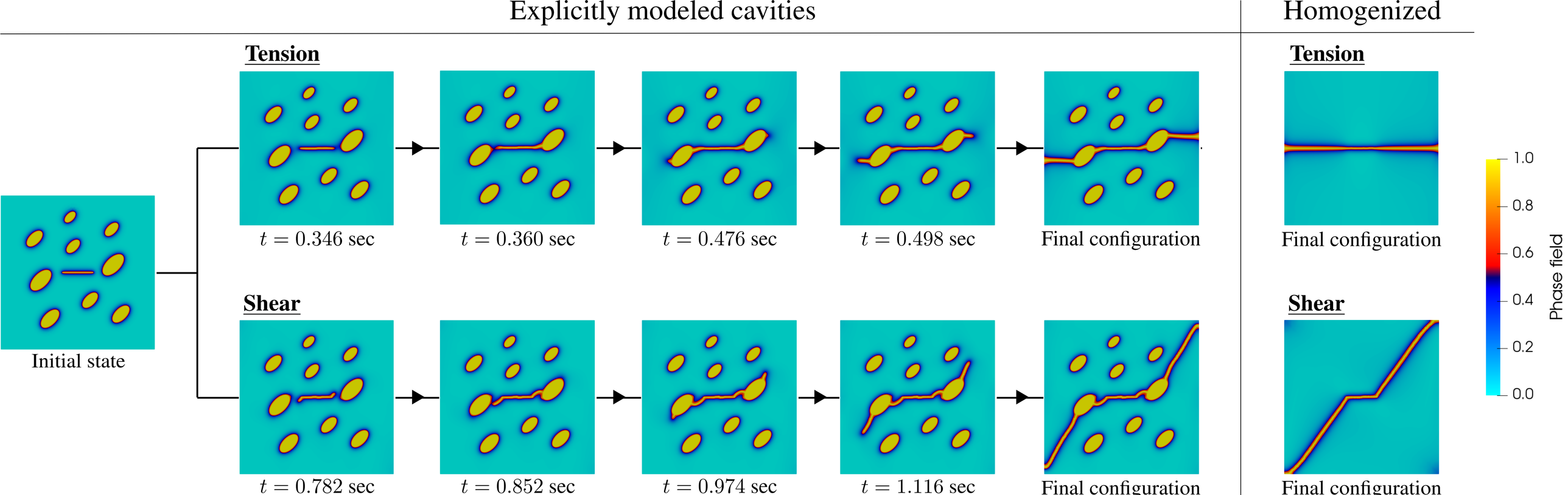
Explicitly modeled cavities
Homogenized
Tension
Initial state
$t = 0.346$ sec
$t = 0.360$ sec
$t = 0.476$ sec
$t = 0.498$ sec
Final configuration
Shear
$t = 0.782$ sec
$t = 0.852$ sec
$t = 0.974$ sec
$t = 1.116$ sec
Final configuration
Tension
Final configuration
Shear
Final configuration
1.0
0.8
0.6
0.4
0.2
0.0
Phase field

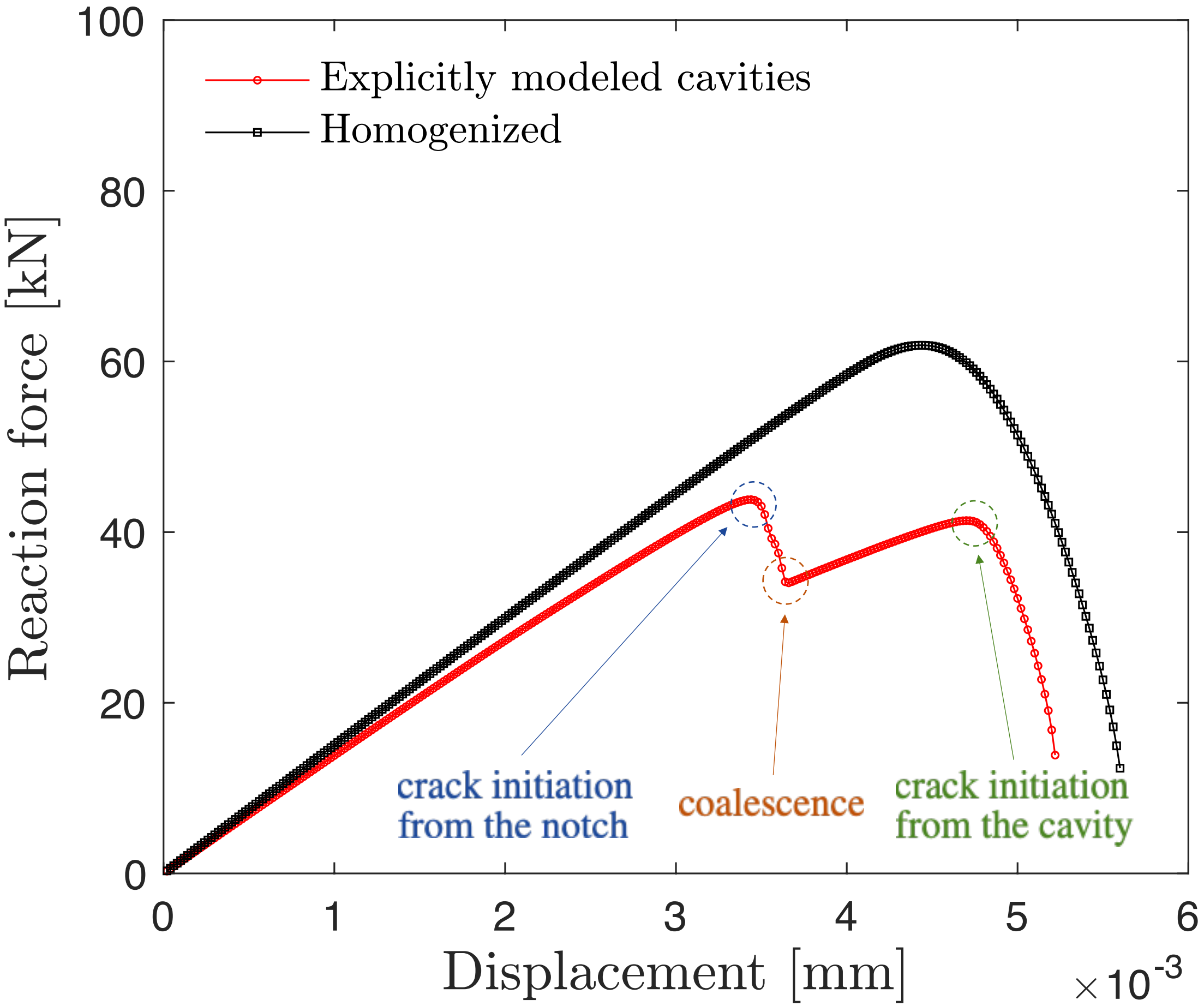
Explicitly modeled cavities
Homogenized
Reaction force [kN]
Displacement [mm]
$\times 10^{-3}$
0
20
40
60
80
100
0
1
2
3
4
5
6
crack initiation
from the notch
coalescence
crack initiation
from the cavity

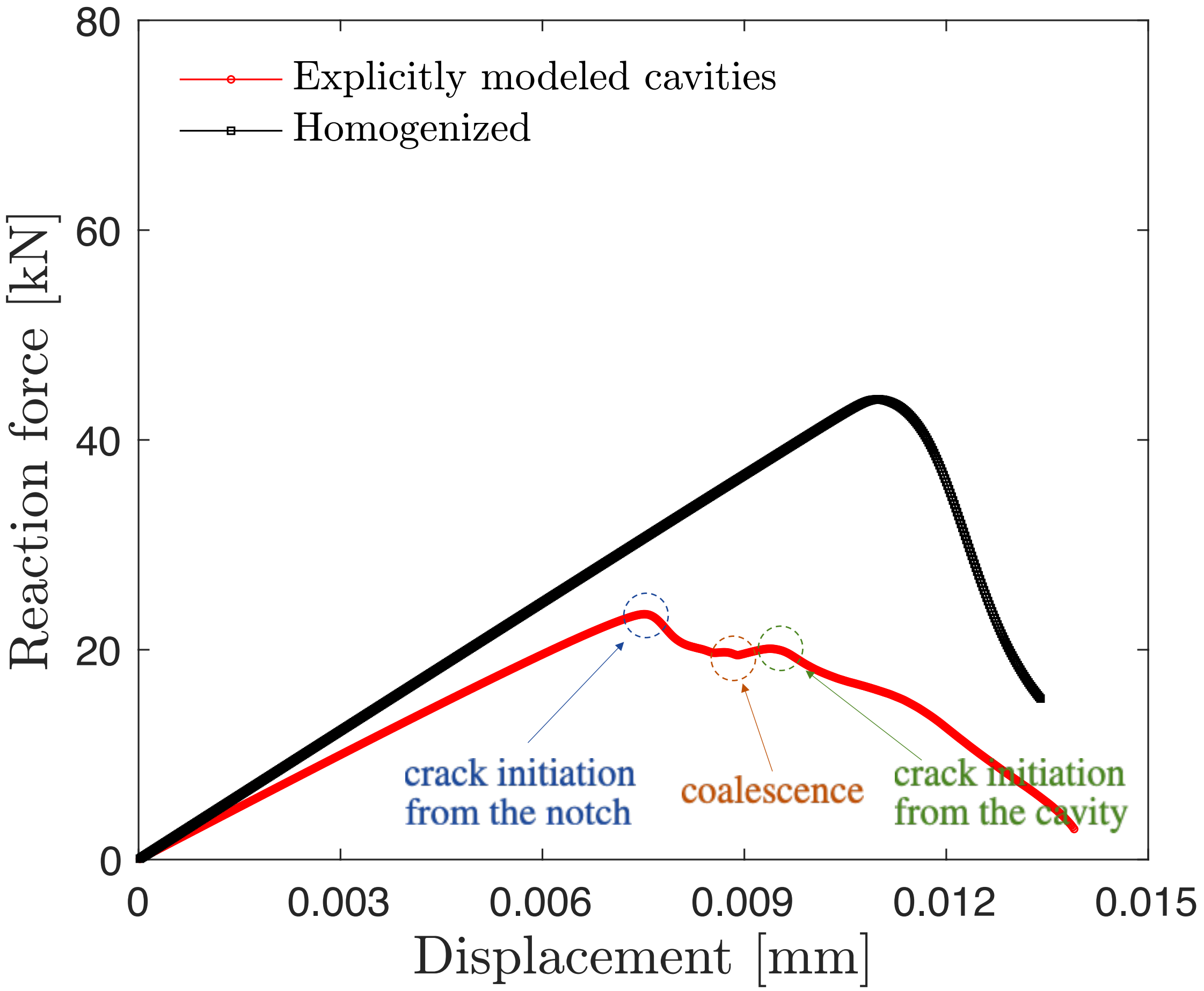
Explicitly modeled cavities
Homogenized
Reaction force [kN]
Displacement [mm]
80
60
40
20
0
0
0.003
0.006
0.009
0.012
0.015
crack initiation
from the notch
coalescence
crack initiation
from the cavity

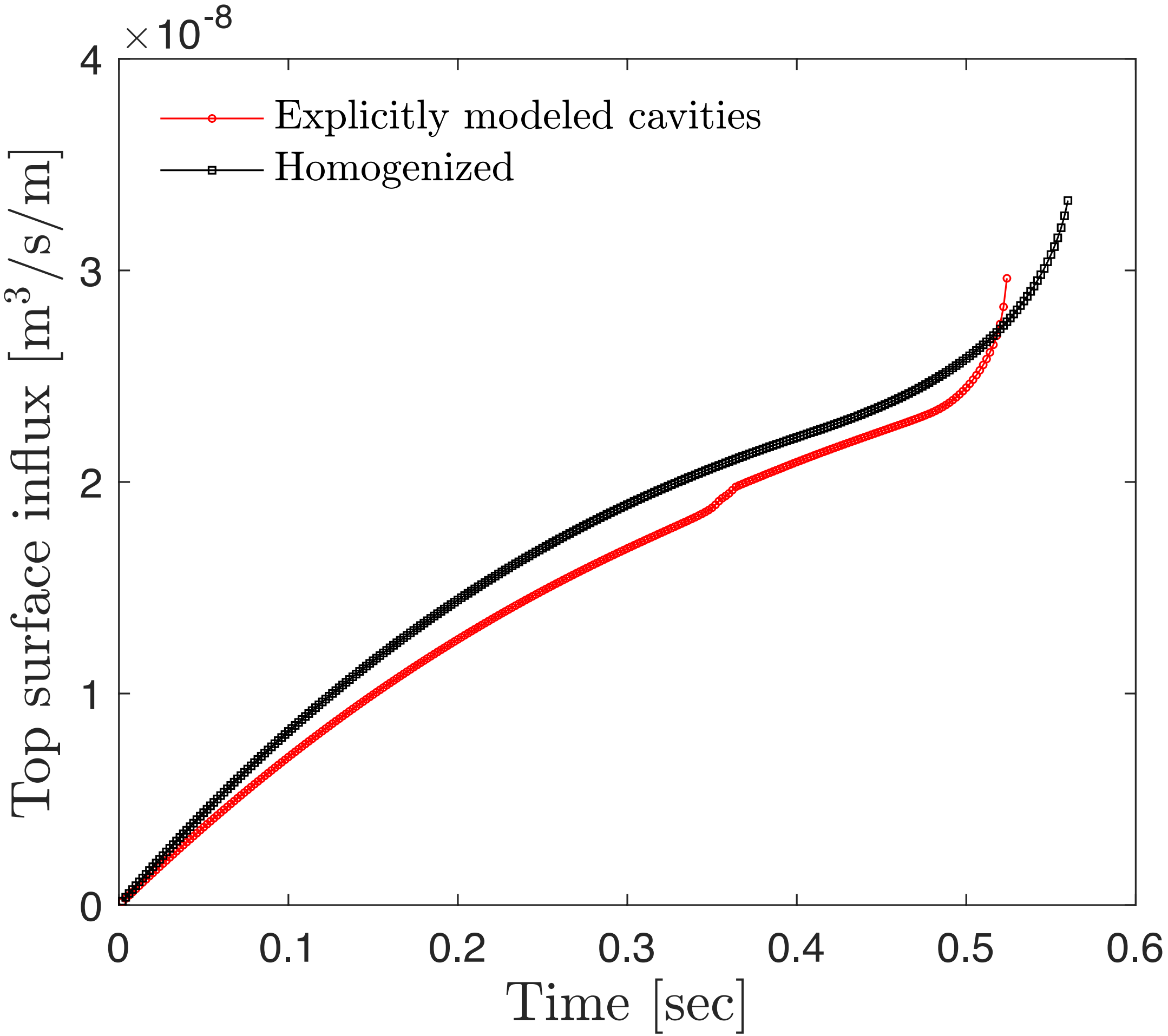
×10^-8
4
3
2
1
0
Explicitly modeled cavities
Homogenized
Top surface influx [m^3/s/m]
0
0.1
0.2
0.3
0.4
0.5
0.6
Time [sec]

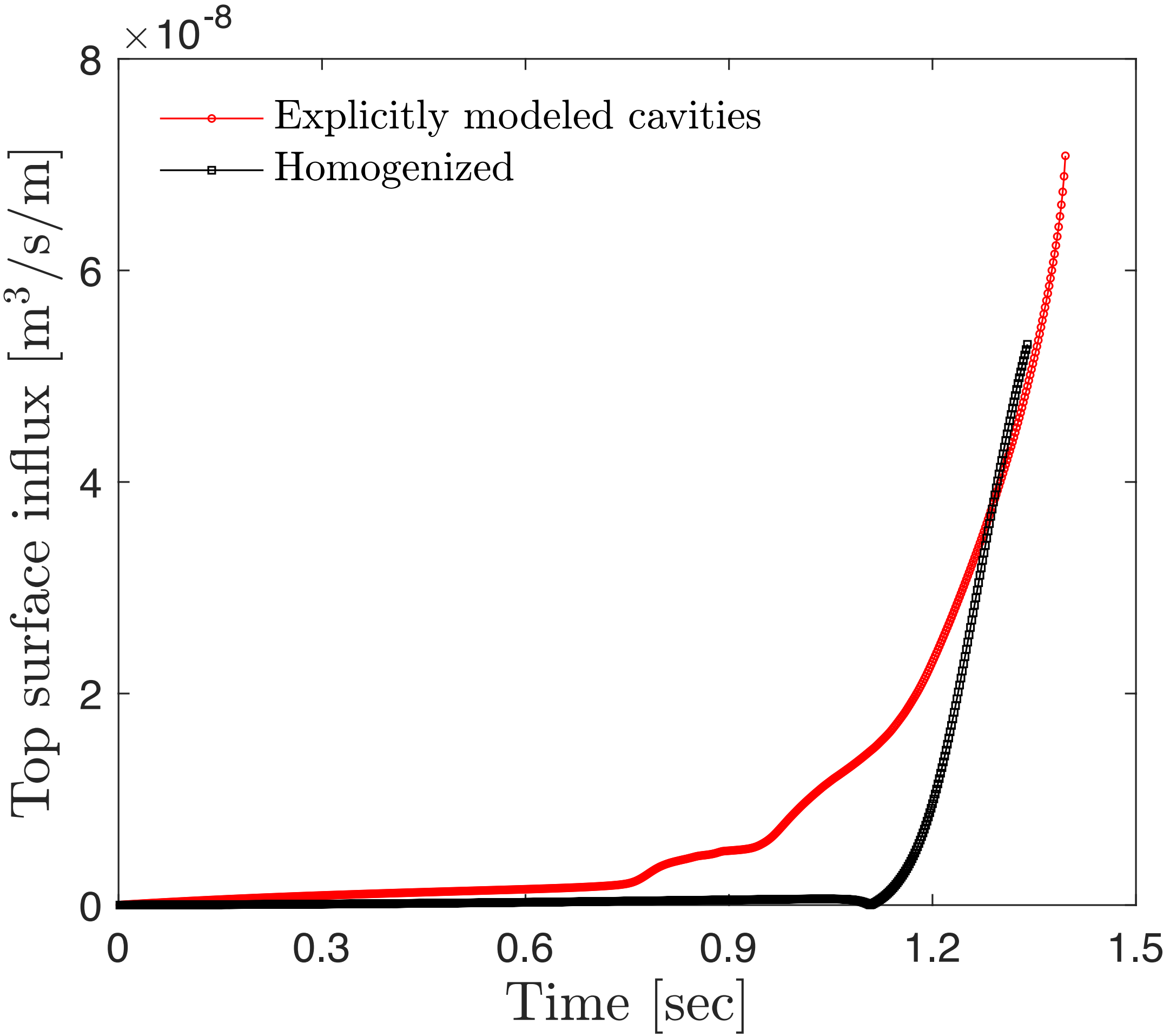
×10^-8
8
6
4
2
0
Explicitly modeled cavities
Homogenized
Top surface influx [m^3/s/m]
0
0.3
0.6
0.9
1.2
1.5
Time [sec]

Tension | **Shear**